nature energy

SUPPLEMENTARY INFORMATION

https://doi.org/10.1038/s41560-020-0607-8

In the format provided by the authors and unedited.

Efficient electrically powered CO_2-to-ethanol via suppression of deoxygenation

Xue Wang[1,10], Ziyun Wang[1,10], F. Pelayo García de Arquer[1], Cao-Thang Dinh[1], Adnan Ozden[2], Yuguang C. Li[1], Dae-Hyun Nam[1], Jun Li[1,2], Yi-Sheng Liu[3], Joshua Wicks[1], Zitao Chen[4], Miaofang Chi[4], Bin Chen[1], Ying Wang[1], Jason Tam[5], Jane Y. Howe[5], Andrew Proppe[1,6], Petar Todorović[1], Fengwang Li[1], Tao-Tao Zhuang[1], Christine M. Gabardo[2], Ahmad R. Kirmani[7], Christopher McCallum[2], Sung-Fu Hung[1], Yanwei Lum[1], Mingchuan Luo[1], Yimeng Min[1], Aoni Xu[1], Colin P. O'Brien[2], Bello Stephen[8], Bin Sun[1], Alexander H. Ip[1], Lee J. Richter[7], Shana O. Kelley[4,9], David Sinton[2] and Edward H. Sargent[1]✉

[1]Department of Electrical and Computer Engineering, University of Toronto, Toronto, Ontario, Canada. [2]Department of Mechanical and Industrial Engineering, University of Toronto, Toronto, Ontario, Canada. [3]Advanced Light Source, Lawrence Berkeley National Laboratory, Berkeley, CA, USA. [4]Center for Nanophase Materials Sciences, Oak Ridge National Laboratory, Oak Ridge, TN, USA. [5]Department of Materials Science and Engineering, University of Toronto, Toronto, Ontario, Canada. [6]Department of Chemistry, University of Toronto, Toronto, Ontario, Canada. [7]Materials Science and Engineering Division, National Institute of Standards and Technology (NIST), Gaithersburg, MD, USA. [8]Hitachi HTA Microscopy Lab, Hillsboro, OR, USA. [9]Department of Pharmaceutical Sciences, Leslie Dan Faculty of Pharmacy, University of Toronto, Toronto, Ontario, Canada. [10]These authors contributed equally: Xue Wang, Ziyun Wang. ✉e-mail: ted.sargent@utoronto.ca

Supplementary Information

Efficient electrically-powered CO_2-to-ethanol via suppression of deoxygenation

Xue Wang[1†], Ziyun Wang[1†], F. Pelayo García de Arquer[1], Cao-Thang Dinh[1], Adnan Ozden[2], Yuguang C. Li[1], Dae-Hyun Nam[1], Jun Li[1,2], Yi-Sheng Liu[3], Joshua Wicks[1], Zitao Chen[4], Miaofang Chi[4], Bin Chen[1], Ying Wang[1], Jason Tam[5], Jane Y. Howe[5], Andrew Proppe[1,6], Petar Todorović[1], Fengwang Li[1], Tao-Tao Zhuang[1], Christine M. Gabardo[2], Ahmad R. Kirmani[7††], Christopher McCallum[2], Sung-Fu Hung[1], Yanwei Lum[1], Mingchuan Luo[1], Yimeng Min[1], Aoni Xu[1], Colin P. O'Brien[2], Bello Stephen[8], Bin Sun[1], Alexander H. Ip[1], Lee J. Richter[7], Shana O. Kelley[4,9], David Sinton[2], Edward H. Sargent[1]*

[1]*Department of Electrical and Computer Engineering, University of Toronto, Toronto, Ontario, Canada.*

[2]*Department of Mechanical and Industrial Engineering, University of Toronto, Toronto, Ontario, Canada.*

[3]*Advanced Light Source, Lawrence Berkeley National Laboratory, Berkeley, CA, USA.*

[4]*Center for Nanophase Materials Sciences, Oak Ridge National Laboratory, Oak Ridge, TN, USA.*

[5]*Department of Materials Science and Engineering, University of Toronto, Toronto, Ontario, Canada.*

[6]*Department of Chemistry, University of Toronto, Toronto, Ontario, Canada.*

[7]*Materials Science and Engineering Division, National Institute of Standards and Technology (NIST), Gaithersburg, MD, USA.*

[8]*Hitachi HTA Microscopy Lab, Hillsboro, OR, USA.*

[9]*Department of Pharmaceutical Sciences, Leslie Dan Faculty of Pharmacy, University of Toronto, Toronto, Ontario, Canada.*

[†]These authors contributed equally to this work.

[††]Guest researcher

*Correspondence and requests for materials should be addressed to Edward H. Sargent (ted.sargent@utoronto.ca) (E.H.S.)

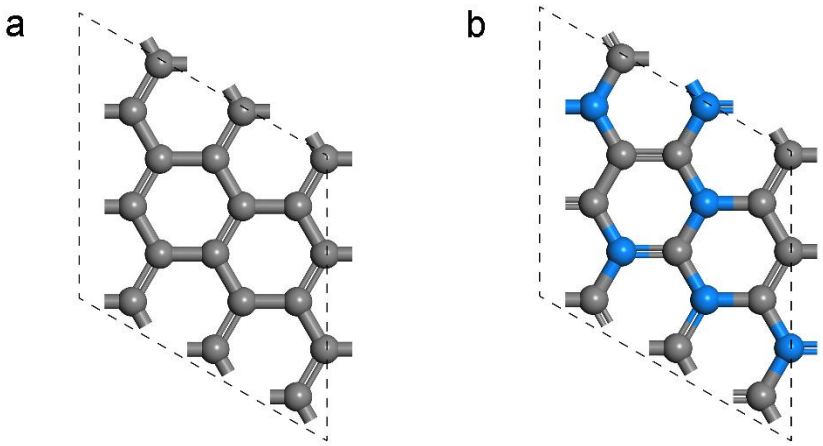

Supplementary Figure 1 | Geometries of carbon and nitrogen-doped carbon layers. a,**b**, Top views of carbon layer (**a**) and nitrogen-doped carbon layer (**b**). Blue and grey balls stand for nitrogen and carbon atoms, respectively. These notations are used throughout this document.

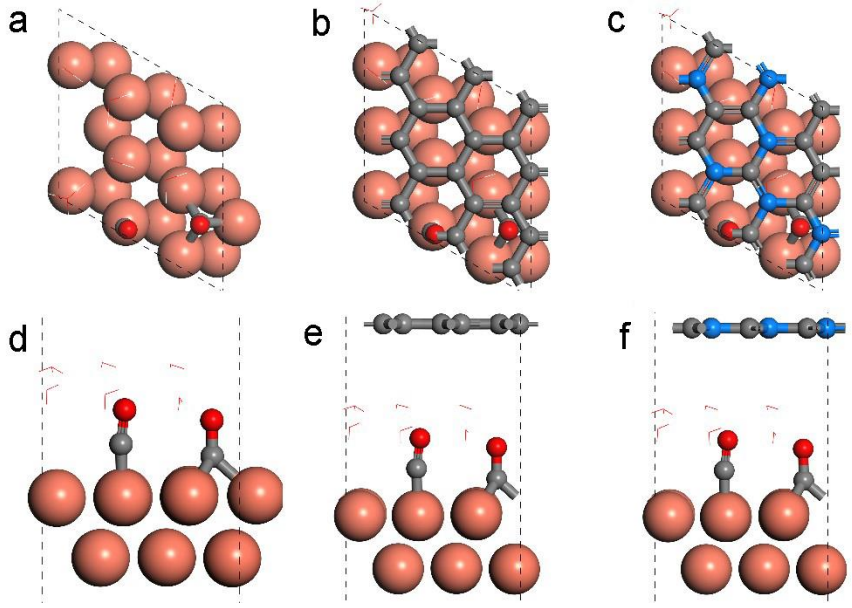

Supplementary Figure 2 | Geometries of CO dimerization initial state. a-c, Top views of CO dimerization initial state on Cu (**a**), Cu with carbon layer (**b**), and Cu with nitrogen-doped carbon layer (**c**). **d-f**, The corresponding side views of CO dimerization initial state on Cu (**d**), Cu with carbon layer (**e**), and Cu with nitrogen-doped carbon layer (**f**). Red, grey, white, orange balls are oxygen, carbon, hydrogen, and copper, respectively. Water molecules are shown as red lines. These notations are used throughout this document. All the Cu models in DFT throughout this work are Cu(111) surface if not specified.

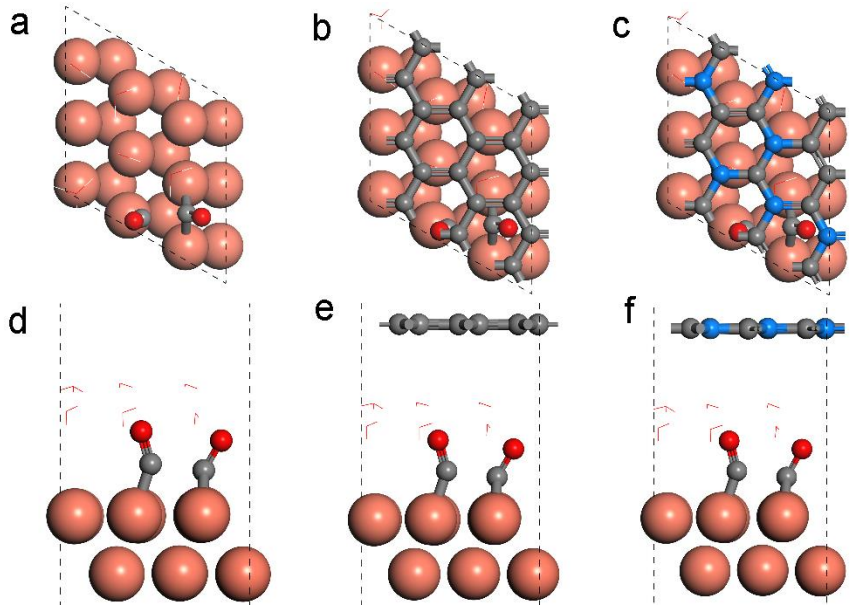

Supplementary Figure 3 | Geometries of CO dimerization transition state. a-c, Top views of CO dimerization transition state on Cu (**a**), Cu with carbon layer (**b**), and Cu with nitrogen-doped carbon layer (**c**). **d-f**, The corresponding side views of CO dimerization initial state on Cu (**d**), Cu with carbon layer (**e**), and Cu with nitrogen-doped carbon layer (**f**).

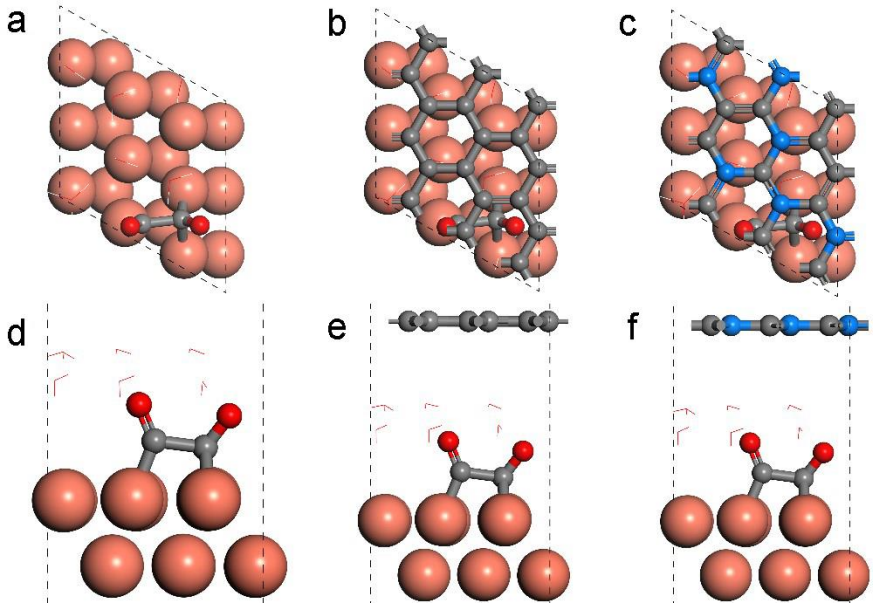

Supplementary Figure 4 | Geometries of CO dimerization final state. a-c, Top views of CO dimerization transition state on Cu (**a**), Cu with carbon layer (**b**), and Cu with nitrogen-doped carbon layer (**c**). **d-f**, The corresponding side views of CO dimerization initial state on Cu (**d**), Cu with carbon layer (**e**), and Cu with nitrogen-doped carbon layer (**f**).

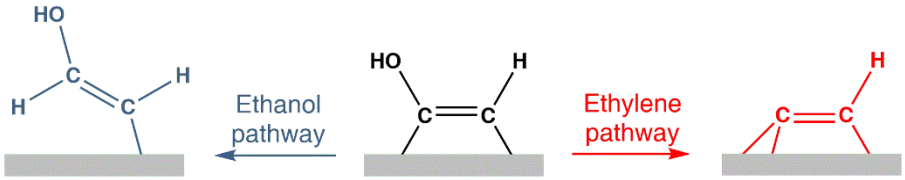

Supplementary Figure 5 | Scheme of ethanol and ethylene pathways.

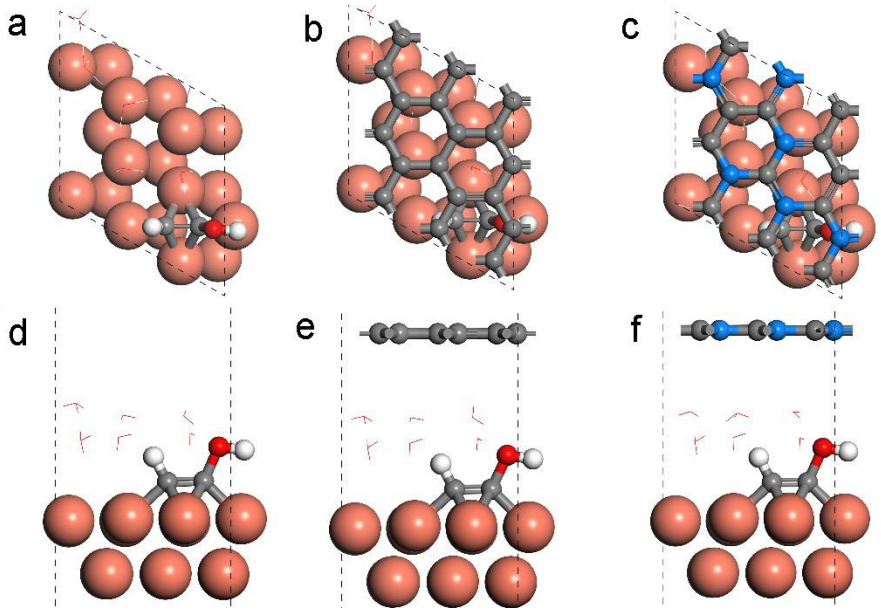

Supplementary Figure 6 | Geometries of key intermediate HOCCH*. a-c, Top views of key intermediate (HOCCH*) branching ethylene and ethanol pathways on Cu (**a**), Cu with carbon layer (**b**), and Cu with nitrogen-doped carbon layer (**c**). **d-f**, The corresponding side views of key intermediate (HOCCH*) branching ethylene and ethanol pathway on Cu (**d**), Cu with carbon layer (**e**), and Cu with nitrogen-doped carbon layer (**f**).

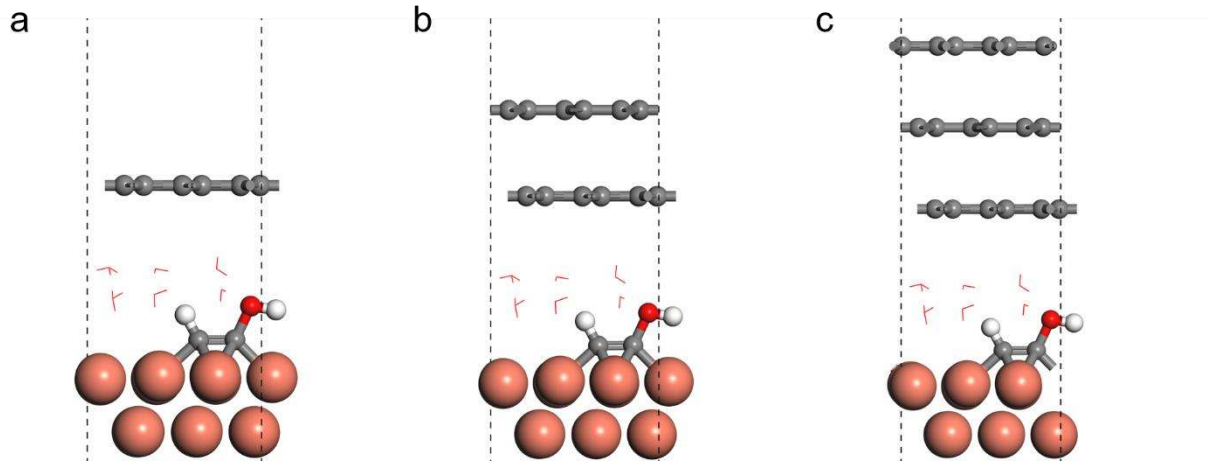

Supplementary Figure 7 | Geometries of intermediate HOCCH* on Cu(111) with different layers of graphite: one layer (a), two layers (b), and three layers (c).

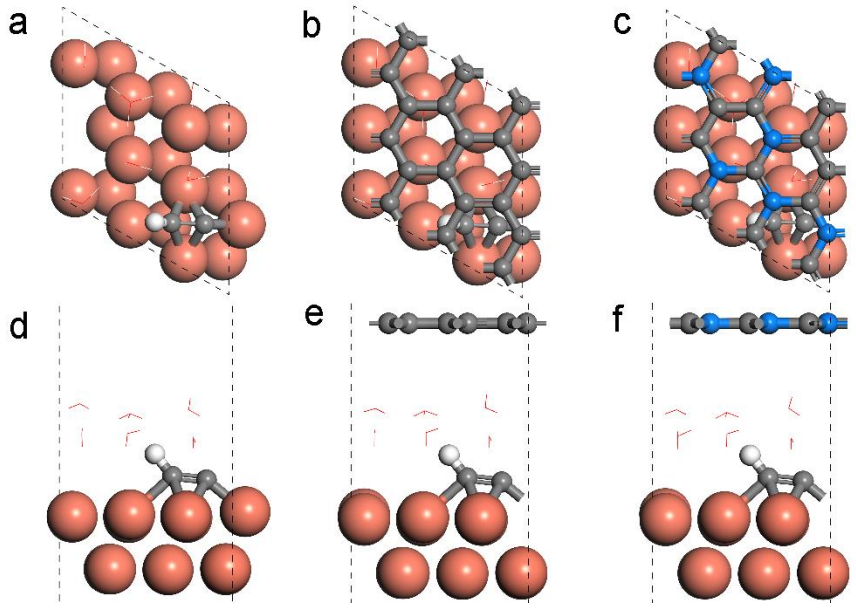

Supplementary Figure 8 | Geometries of the intermediate CCH*. a-c, Top views of the intermediate (CCH*) in ethylene pathway on Cu (**a**), Cu with carbon layer (**b**), and Cu with nitrogen-doped carbon layer (**c**). **d-f**, The corresponding side views of the intermediate (CCH*) in ethylene pathway on Cu (**d**), Cu with carbon layer (**e**), and Cu with nitrogen-doped carbon layer (**f**).

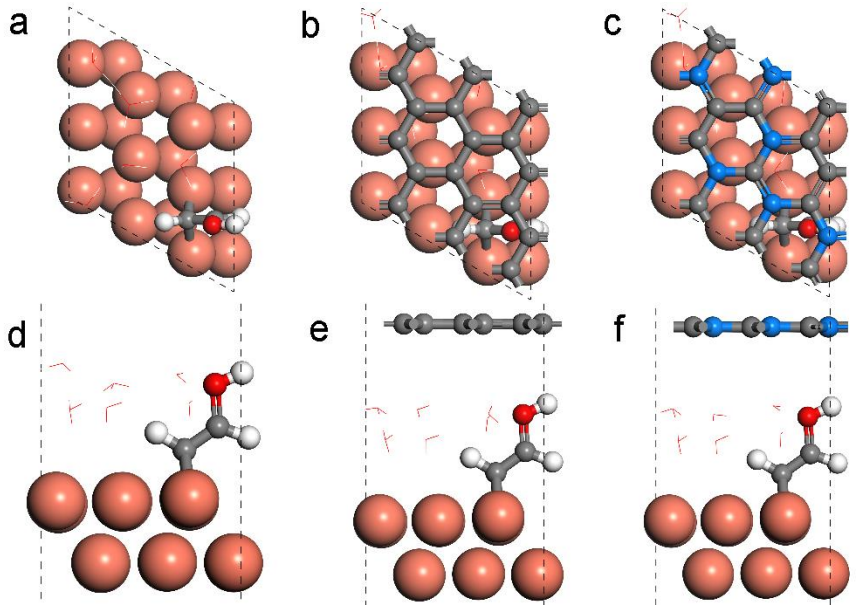

Supplementary Figure 9 | Geometries of the intermediate HOCHCH*. a-c, Top views of the intermediate (HOCHCH*) in ethanol pathway on Cu (**a**), Cu with carbon layer (**b**), and Cu with nitrogen-doped carbon layer (**c**). **d-f**, The corresponding side views of the intermediate (HOCHCH*) in ethanol pathway on Cu (**d**), Cu with carbon layer (**e**), and Cu with nitrogen-doped carbon layer (**f**).

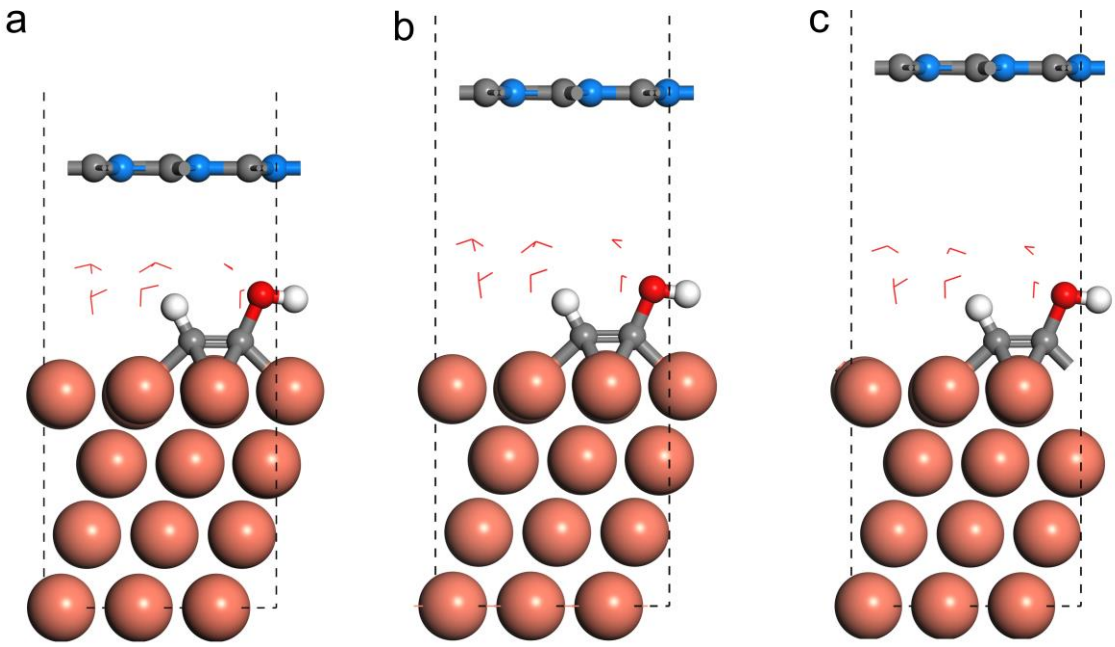

Supplementary Figure 10 | Geometries of key intermediate HOCCH* with different distances between N-C layer and Cu layer ($d_{N\text{-}C/Cu}$) with two adsorbed *CO and one charged water layer. a, $d_{N\text{-}C/Cu}$ = 6.42 Å. **b**, $d_{N\text{-}C/Cu}$ = 8.42 Å. **c**, $d_{N\text{-}C/Cu}$ = 9.42 Å.

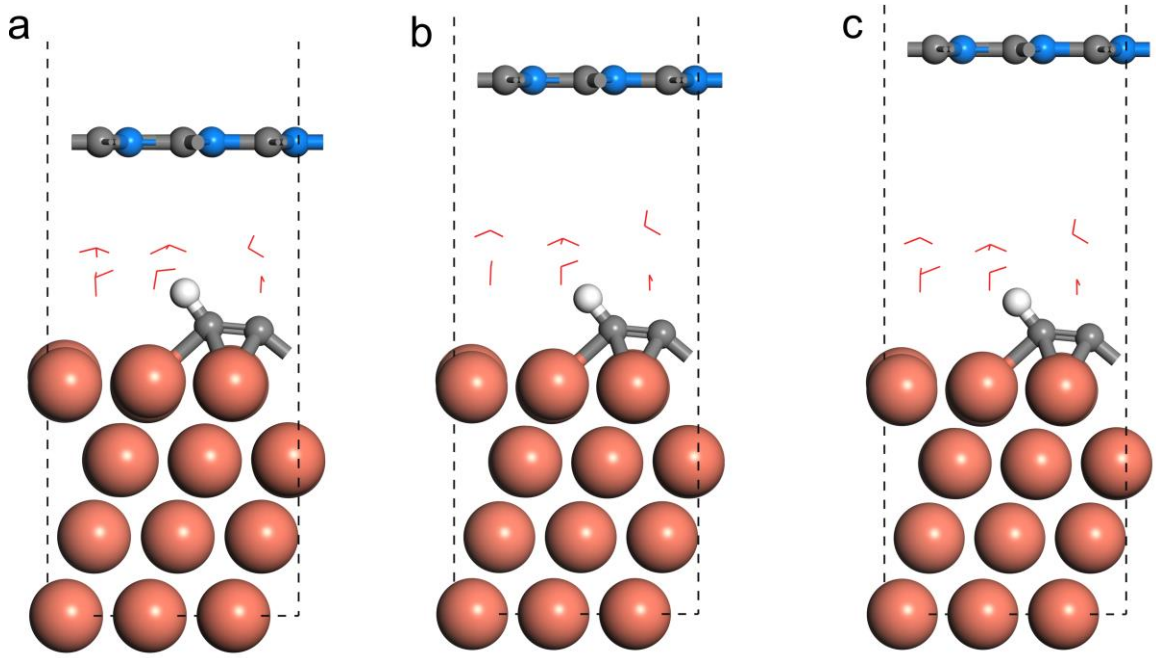

Supplementary Figure 11 | Geometries of the intermediate CCH* with difference $d_{N\text{-}C/Cu}$ with two adsorbed *CO and one charged water layer. a, $d_{N\text{-}C/Cu}$ = 6.42 Å. **b**, $d_{N\text{-}C/Cu}$ = 8.42 Å. **c**, $d_{N\text{-}C/Cu}$ = 9.42 Å.

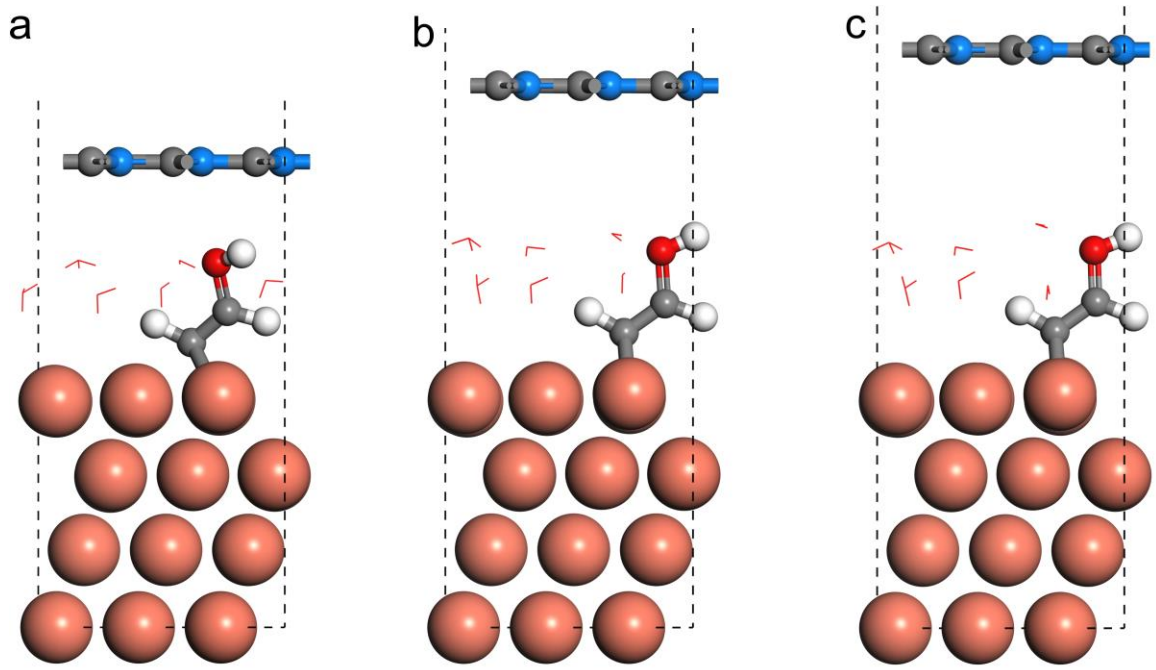

Supplementary Figure 12 | Geometries of the intermediate HOCHCH* with difference $d_{N\text{-}C/Cu}$ with two adsorbed *CO and one charged water layer. a, $d_{N\text{-}C/Cu}$ = 6.42 Å. **b**, $d_{N\text{-}C/Cu}$ = 8.42 Å. **c**, $d_{N\text{-}C/Cu}$ = 9.42 Å.

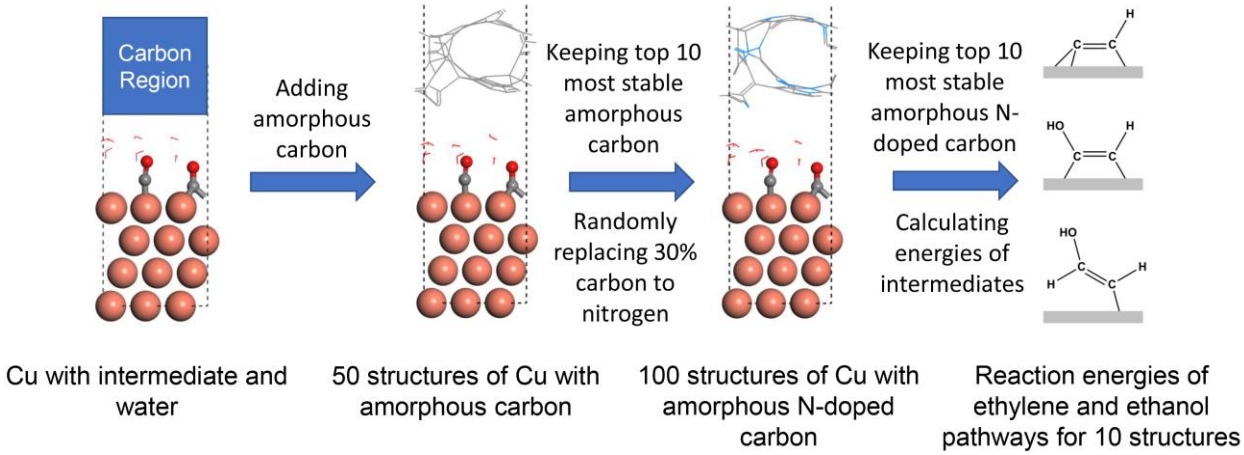

Supplementary Figure 13 | Pipeline for the generation of amorphous N-doped carbon structures.

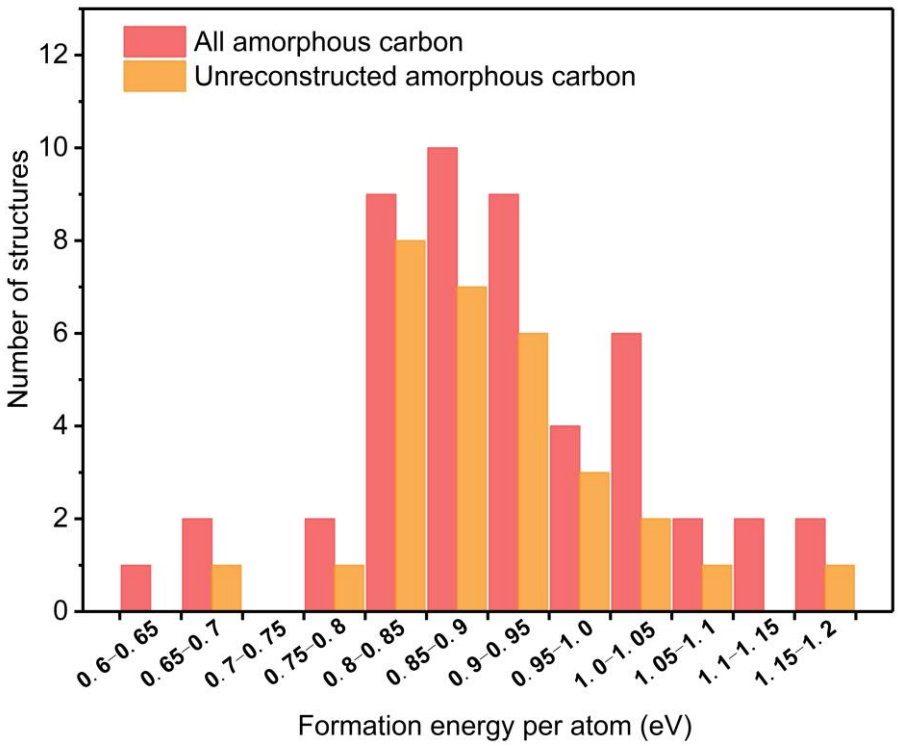

Supplementary Figure 14 | Distribution of formation energy per atom for amorphous carbon on the Cu surface. Intermediates and water are taken into account**.** The distribution of all vs. unreconstructed amorphous structures are shown in red and orange, respectively.

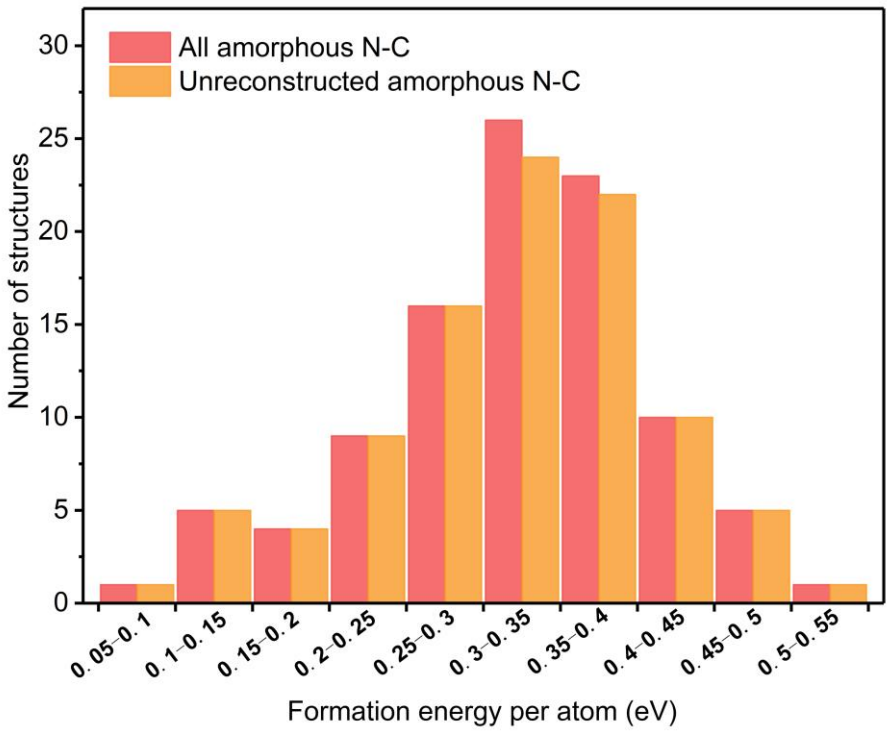

Supplementary Figure 15 | Distribution of formation energy per atom for amorphous N-doped carbon on the Cu. Intermediates and water are taken into account. The distribution of all vs. unreconstructed amorphous structures are shown in red and orange, respectively.

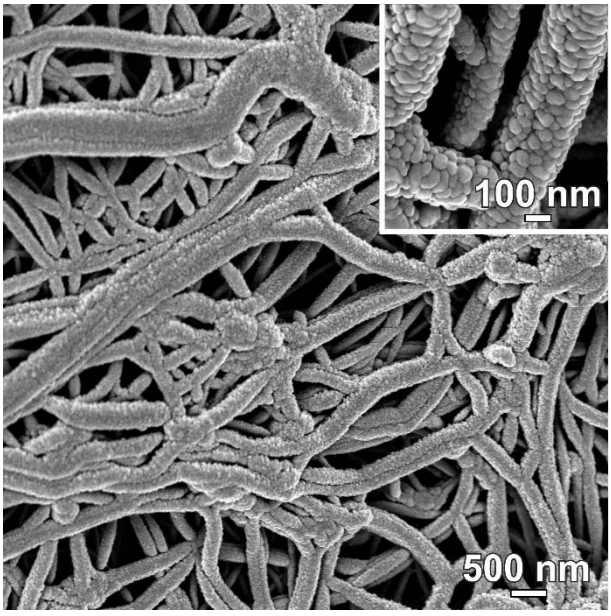

Supplementary Figure 16 | SEM image of sputtered Cu on PTFE.

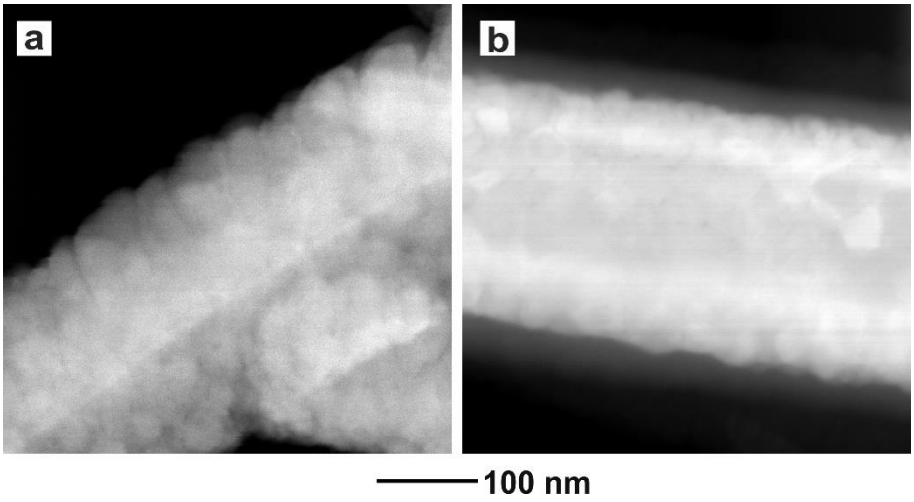

Supplementary Figure 17 | HAADF-STEM images of Cu-PTFE (a) and 34% N-C/Cu-PTFE (b).

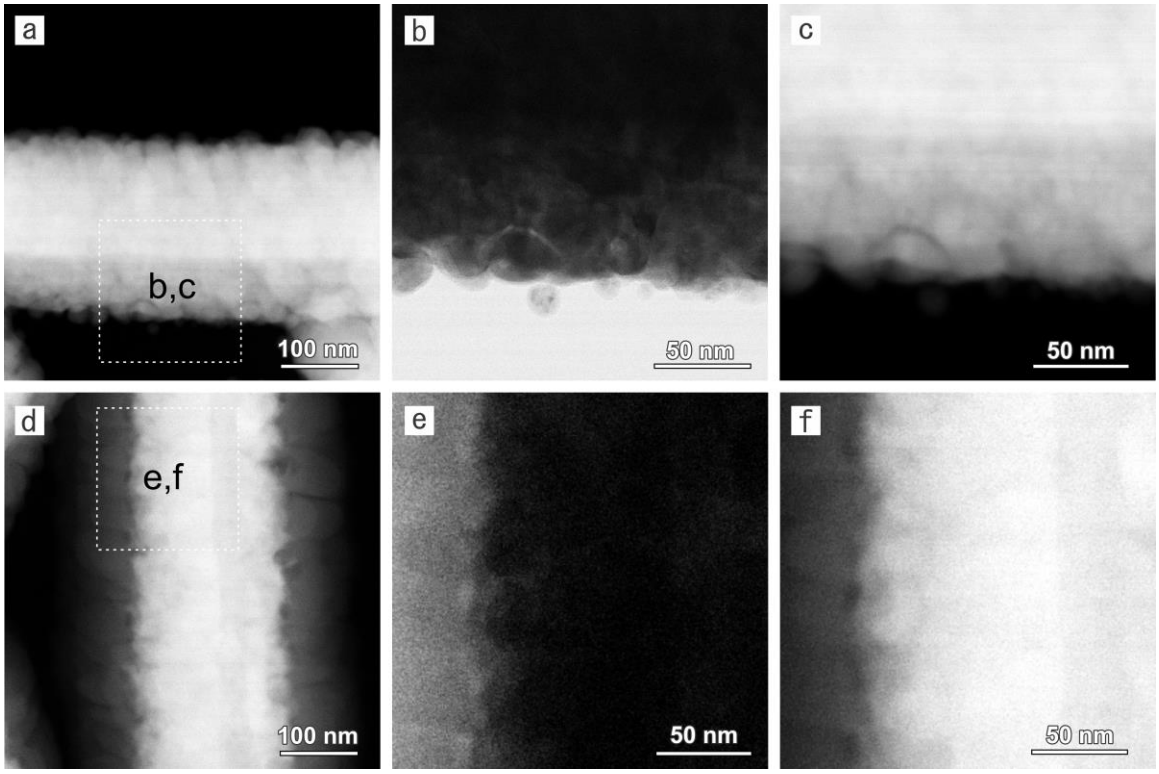

Supplementary Figure 18 | Structural analysis of Cu-PTFE and 34% N-C/Cu-PTFE. a-c, HAADF-STEM image of Cu-PTFE (**a**) and higher magnification bright field STEM (**b**) and the corresponding HAADF-STEM image (**c**) taken from the area marked by the box in (**a**). **d-f**, HAADF-STEM image of 34% N-C/Cu-PTFE (**d**) and higher magnification bright field STEM (**e**) and the corresponding HAADF-STEM image (**f**) taken from the area marked by the box in (**d**). There is no observable morphology difference on Cu between Cu-PTFE and 34% N-C/Cu-PTFE.

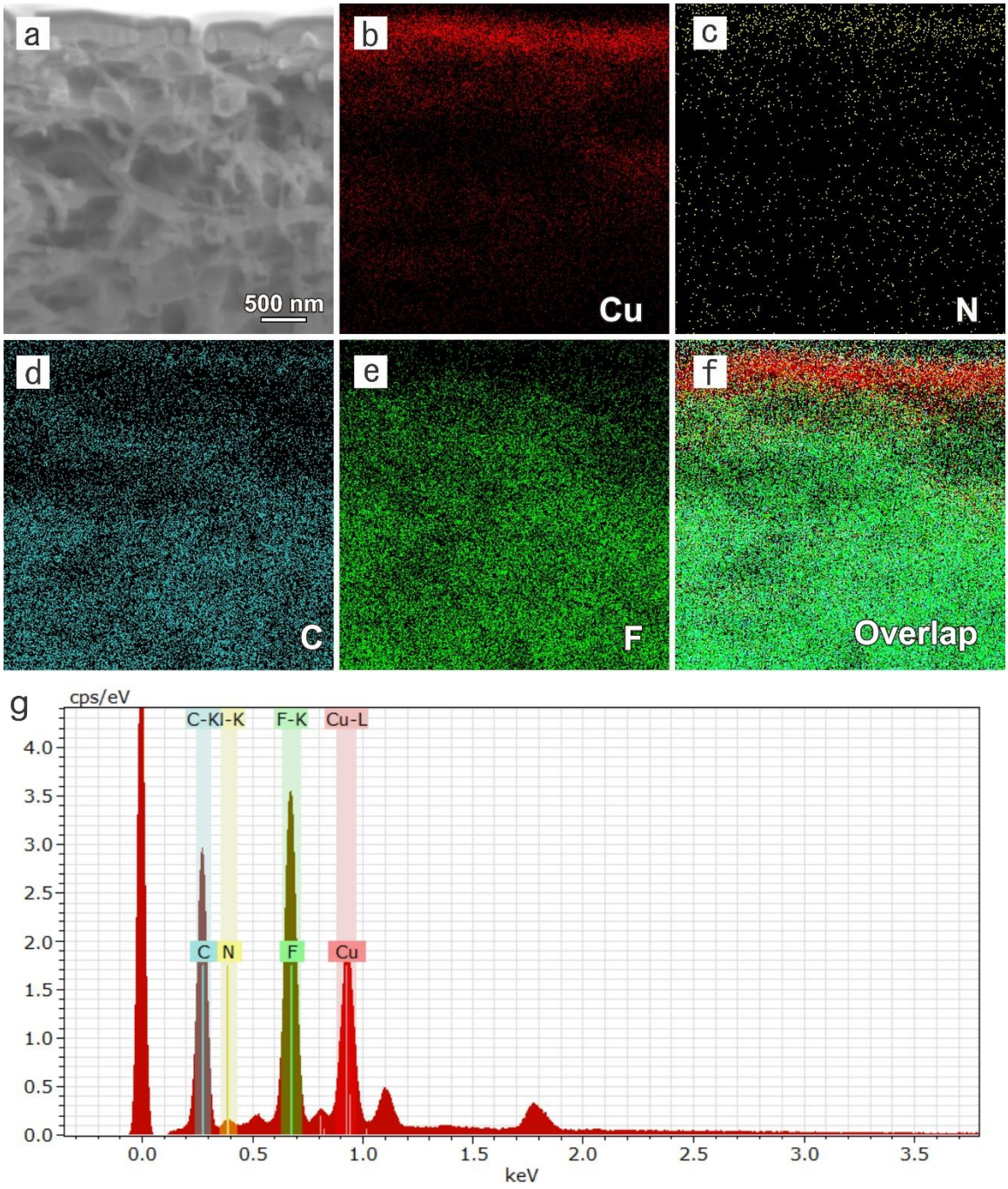

Supplementary Figure 19 | Cross-section characterization for the electrode of 34% N-C/Cu on PTFE. a-g, Cross-section SEM image (**a**), the corresponding EDX elemental mapping of Cu, N, C, and F (**b-f**), and the corresponding EDX analysis (**g**) for 34% N-C/Cu on PTFE. The EDX elemental mapping and EDX analysis of F is used to distinguish PTFE substrate.

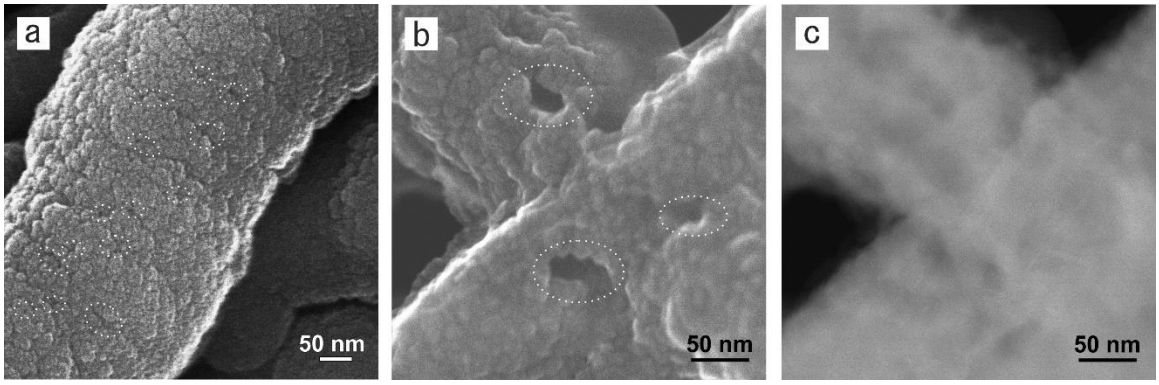

Supplementary Figure 20 | SEM image (a), and secondary electron image (b) and the corresponding HAADF-STEM image (c) of 34% N-C/Cu catalyst on PTFE. The holes on the N-C layer are indicated using dotted lines.

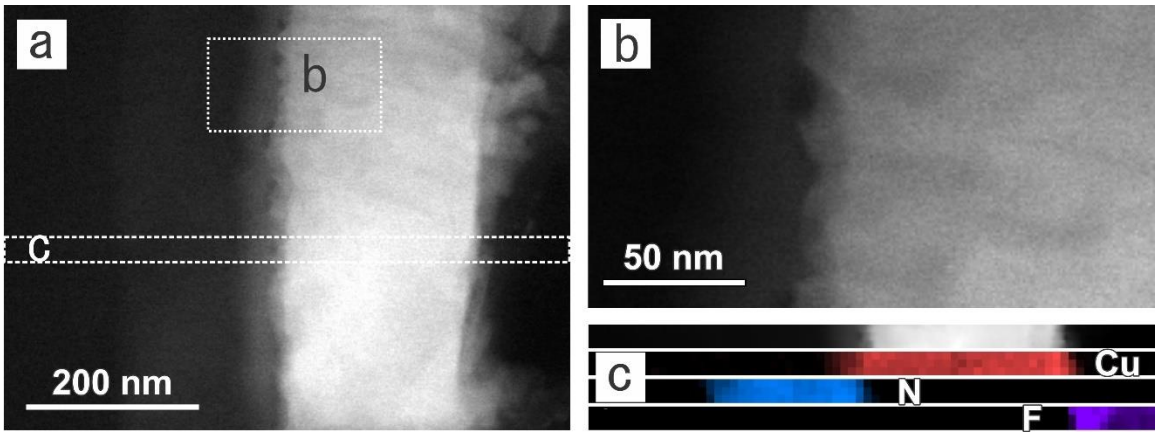

Supplementary Figure 21 | Structural and compositional analyses of the prepared ultrathin slice of 34% N-C/Cu. a, HAADF-STEM image of the 34% N-C/Cu ultrathin slice. **b**, Higher magnification HAADF-STEM image taken from the area marked by a box in (**a**). **c**, HAADF-STEM image of the area marked in (**a**) and the corresponding EELS elemental mappings of Cu, N, and F.

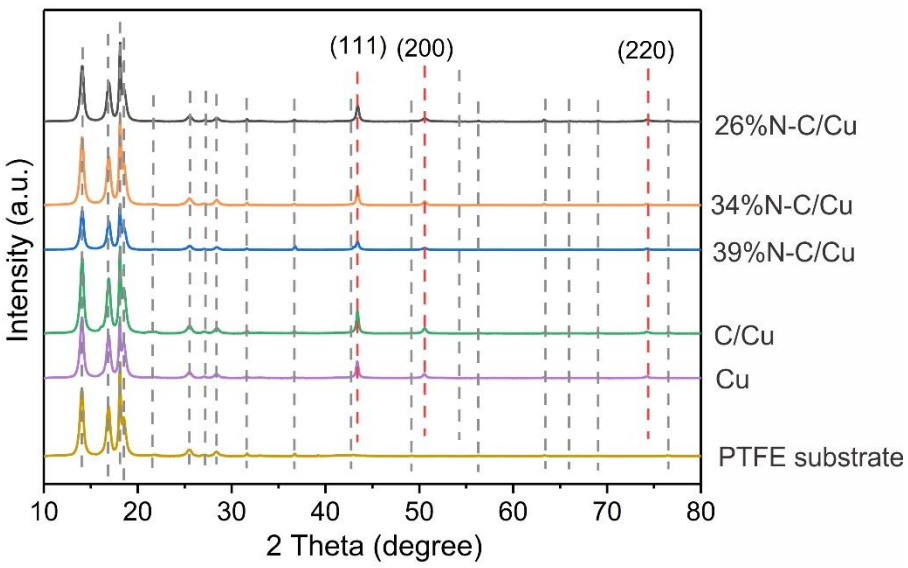

Supplementary Figure 22 | XRD patterns for PTFE substrate and different electrodes. The peaks marked by gray and red dot lines come from PTFE substrate and Cu, respectively.

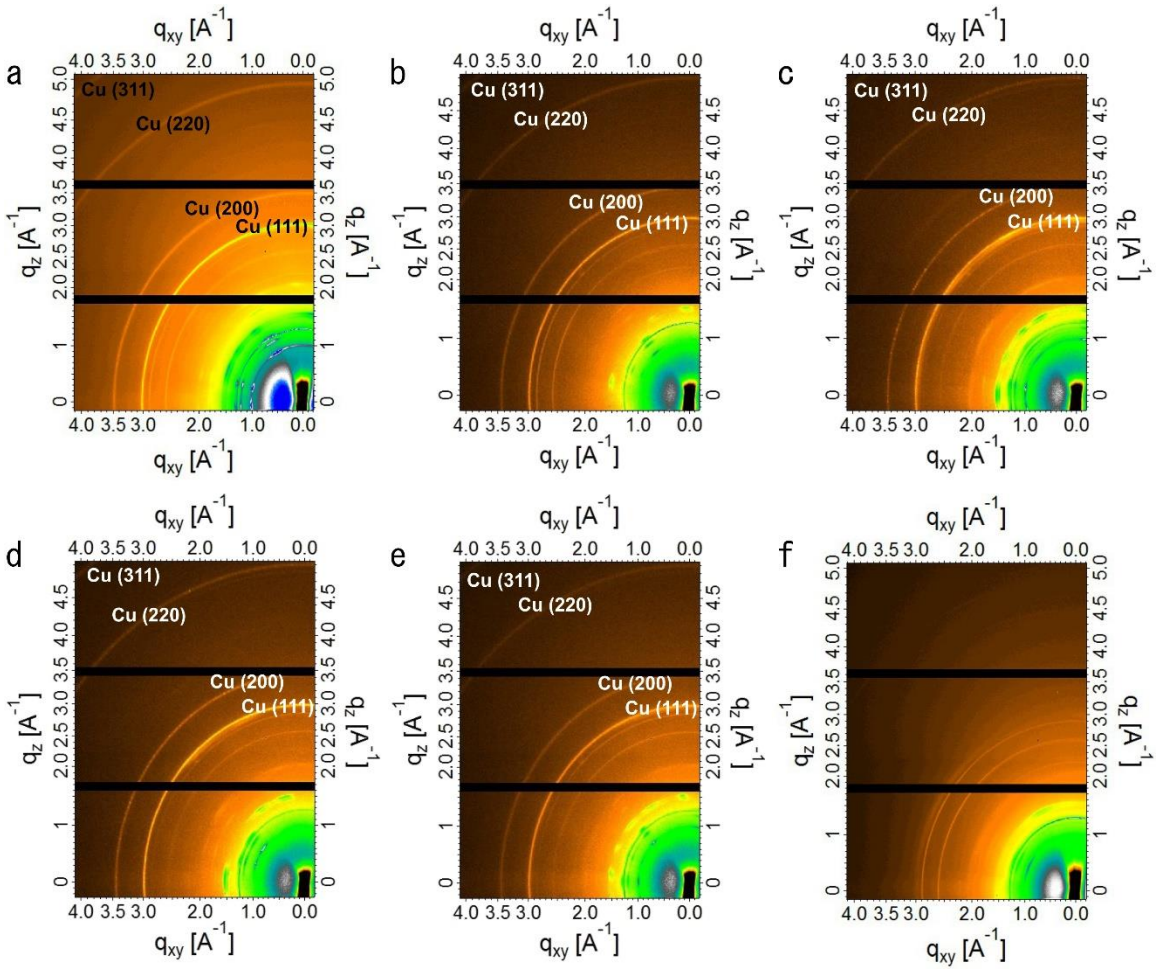

Supplementary Figure 23 | Structural characterization of different electrodes and PTFE substrate. a-e, WAXS maps for 26% N-C/Cu (**a**), 34% N-C/Cu (**b**), 39% N-C/Cu (**c**), C/Cu (**d**), and sputtered Cu (**e**) on PTFE substrates. **f**, WAXS map for PTFE substrate.

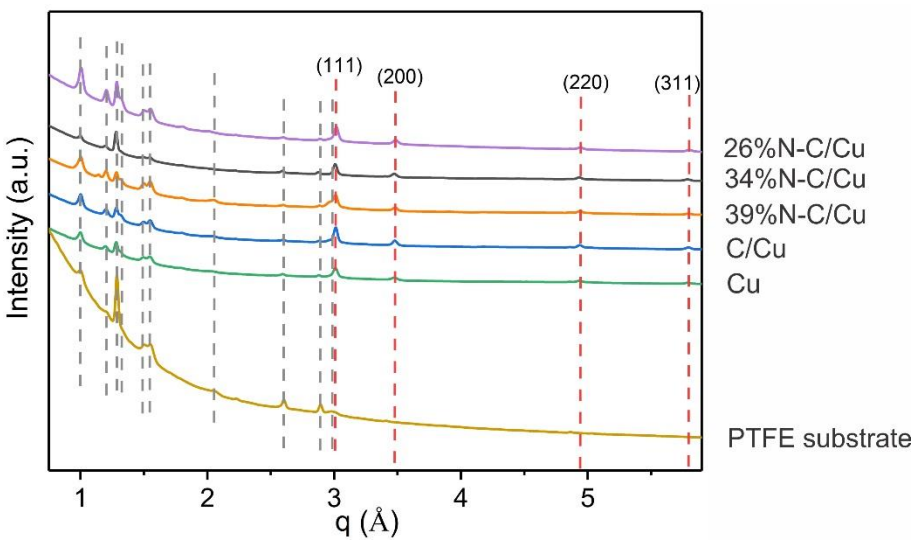

Supplementary Figure 24 | Sector-averages of WAXS maps in Supplementary Fig. 23 for different electrodes and PTFE substrate. The peaks marked by gray and red dot lines come from PTFE substrates and Cu, respectively.

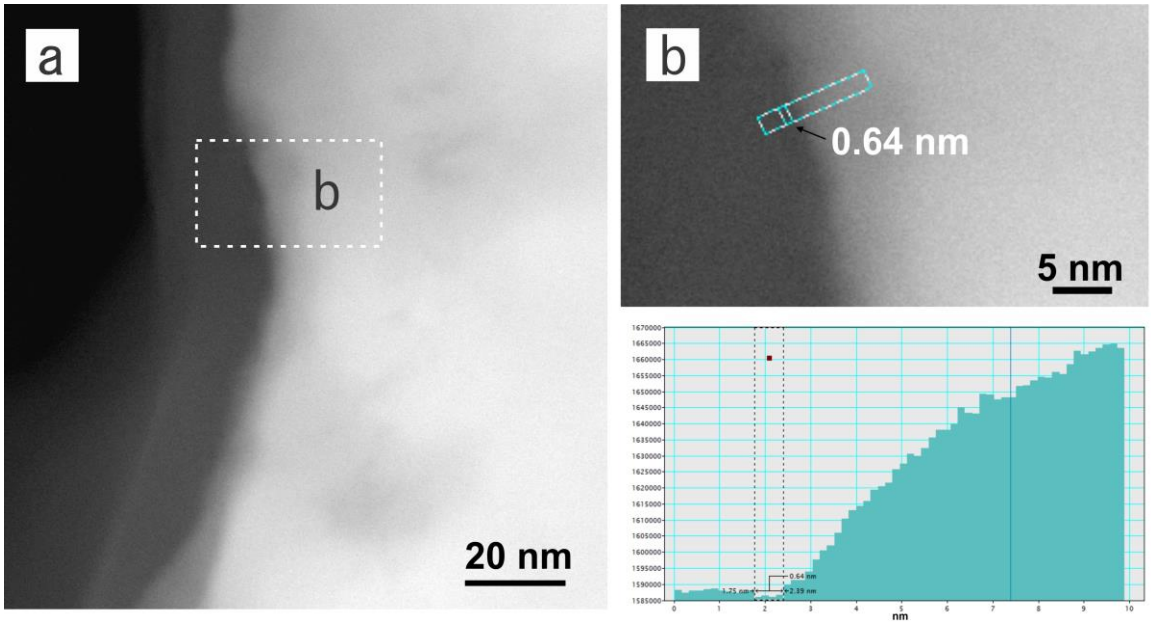

Supplementary Figure 25 | Structural analysis of ultrathin slice of 34% N-C/Cu. a, HAADF-STEM image of the 34% N-C/Cu ultrathin section. **b,** Higher magnification HAADF-STEM image taken from the area marked by the box in (**a**) and its intensity profile taken along the rectangular frame displaying the distances between Cu layer and N-C layer.

The images used for the analysis of the gap are obtained with the camera **not** saturated in any regions of the field surveyed in these images (Fig. 2h,i and Supplementary Fig. 25). The intensity profile of the reduced region thus is used for determining the gap width, by taking the width of the half minimum value. The measurement shows that *the gap between Cu and N-C layers are generally below 1 nm* (Fig. 2h,i and Supplementary Fig. 25). If the N-C layer is closely attached to the Cu layer, one should expect the intensity profile shows a steady increase till the contrast from the Cu layer contribution. The dips in the intensity profiles (Fig. 2i and Supplementary Fig. 25b) on the other hand demonstrate the presence of a small gap between N-C layer and Cu layer.

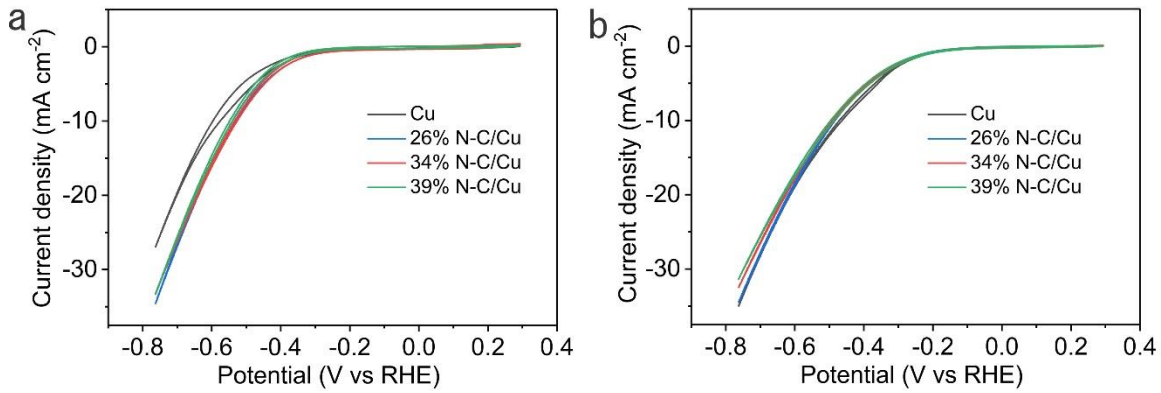

Supplementary Figure 26 | CVs for different samples in 1 M KOH by supplying different gases to gas chamber of the cell. a, N_2. **b**, CO_2.

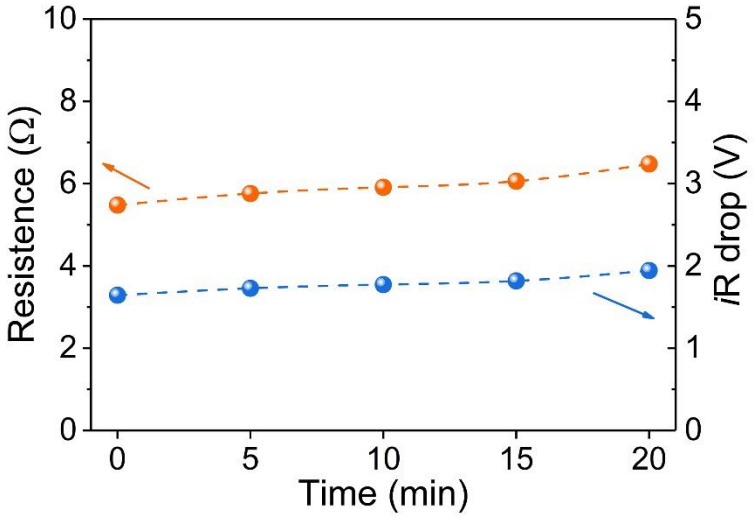

Supplementary Figure 27 | The resistance between the working and reference electrodes determined by EIS technique and the corresponding *i*R drop in the course of the electrolysis at 300 mA cm^{-2}.

We have measured the resistance (R) between the working and reference electrodes with 34% N-C/Cu catalyst in the course of constant-current (300 mA cm^{-2}) electrolysis through electrochemical impedance spectroscopy (EIS) technique, and calculated the corresponding *i*R drop (Supplementary Fig. 27). The results show that both the R and *i*R drop gradually increase during electrolysis, and the resistance increases from 5.5 Ω at the beginning of the electrolysis to 6.5 Ω after 20 min electrolysis. Considering that R increases during the electrolysis, the potential is corrected based on the lowest R – the R at the beginning of the electrolysis.

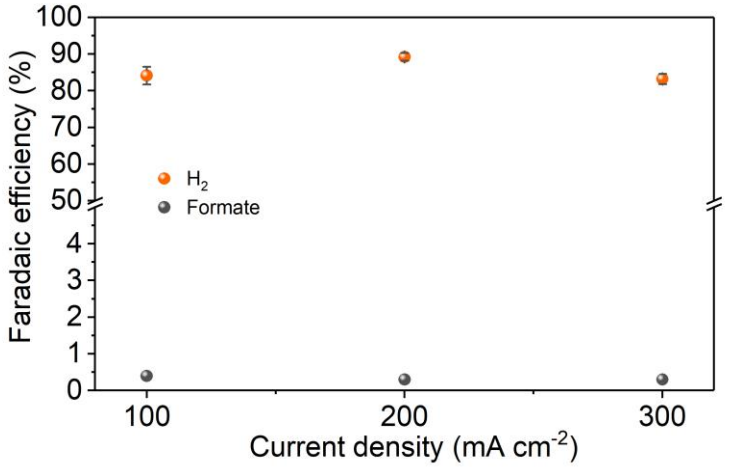

Supplementary Figure 28 | CO_2RR performance of 34% N-C GDE under different current densities. Error bars represent the standard deviation of measurements based on three independent samples.

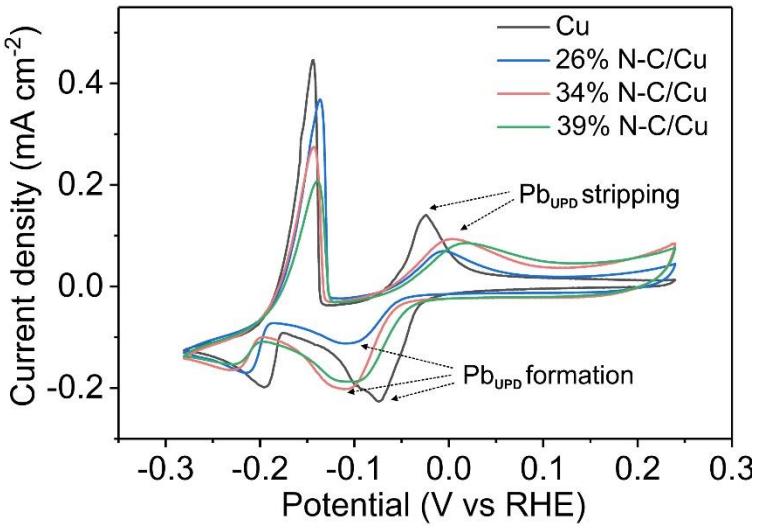

Supplementary Figure 29 | CVs for different samples measured in 100 mM $HClO_4$ + 1 mM $Pd(ClO_4)_2$.

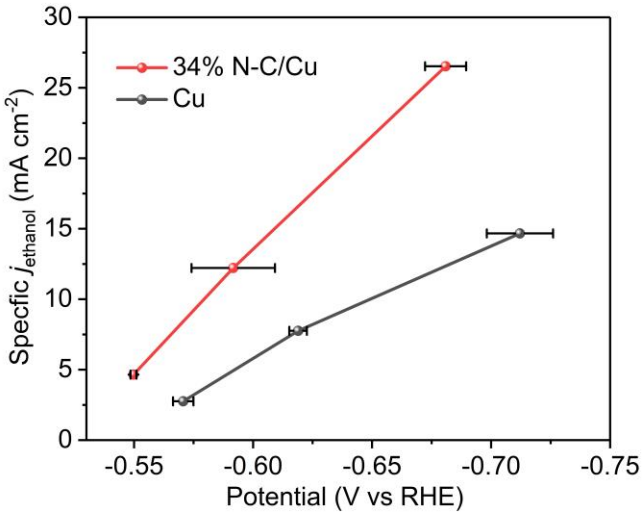

Supplementary Figure 30 | Partial ethanol current density normalized to Cu_{ECSA} for Cu and 34% N-C/Cu catalysts versus potential for CO_2RR. Error bars denote the standard deviation of potentials (n > 300) during the constant-current electrolysis.

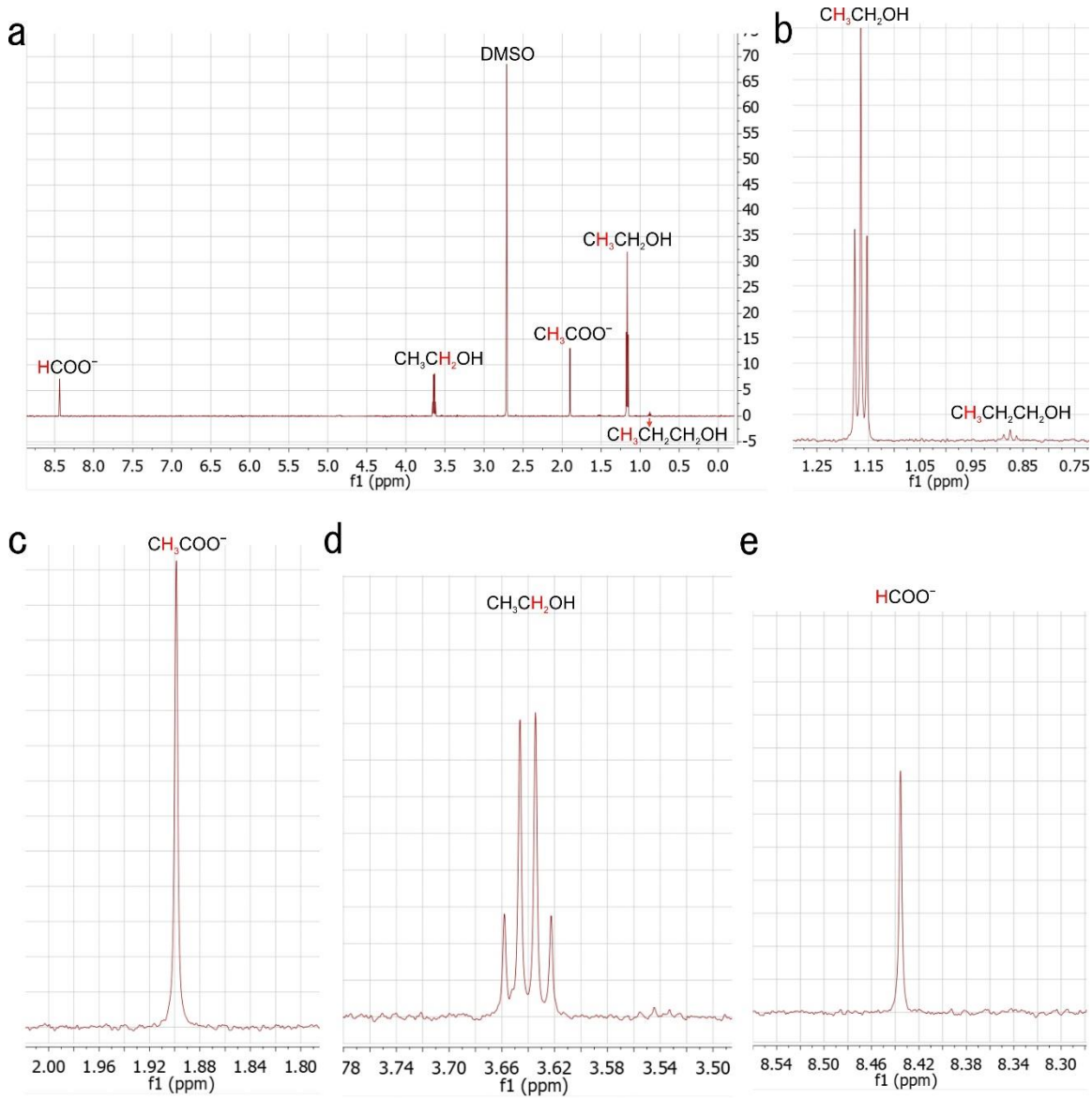

Supplementary Figure 31 | NMR spectra of liquid products. a, Representative ^{1}H-NMR spectrum of catholyte after CO_2RR on 34% N-C/Cu cathodes by applying 300 mA cm^{-2} in 1 M KOH. DMSO is used as an internal standard. **b-e**, The corresponding enlarged ^{1}H-NMR spectra demonstrating ethanol and n-propanol (**b**), acetate (**c**), ethanol (**d**), and formate (**e**).

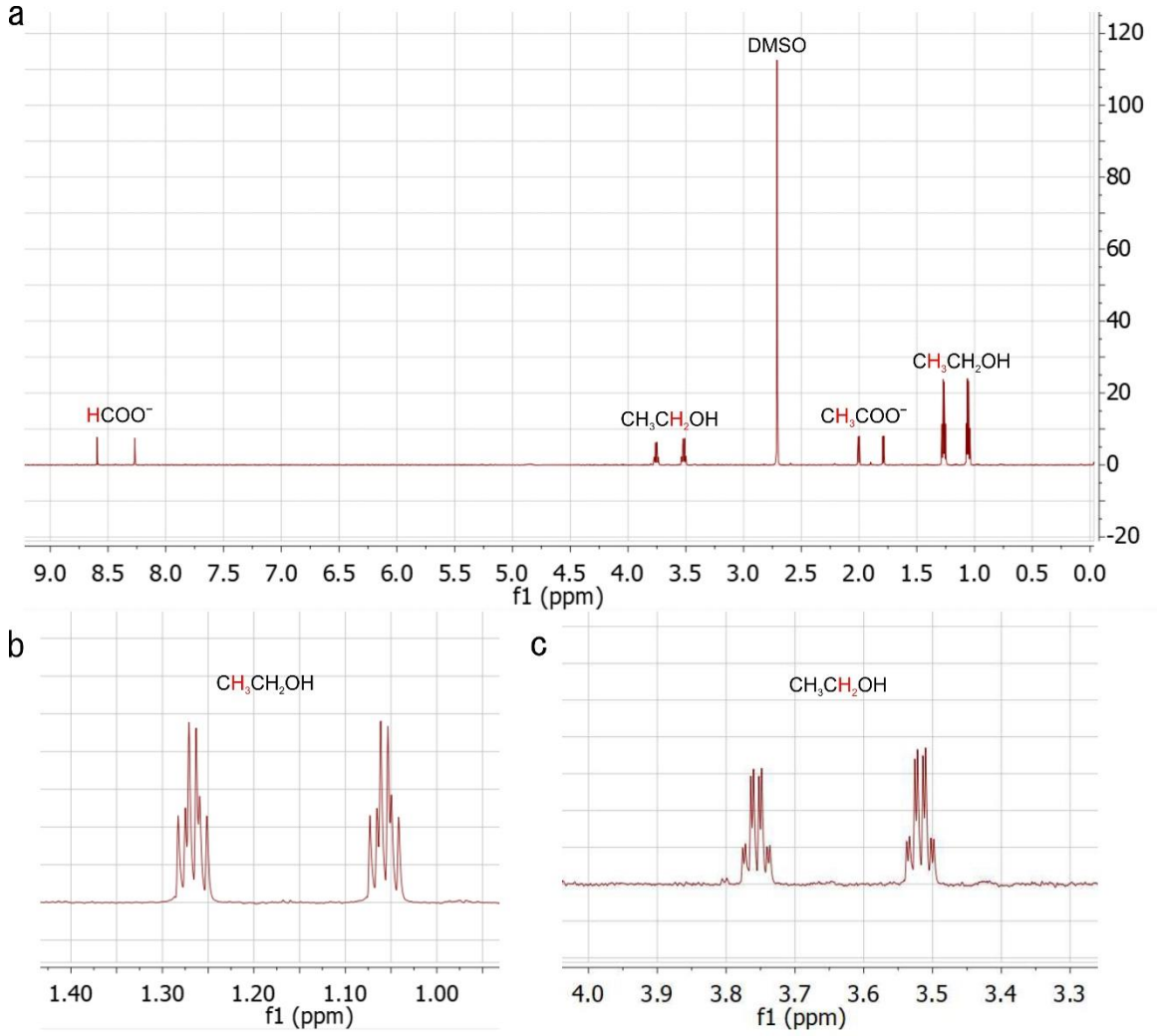

Supplementary Figure 32 | NMR spectra of liquid products obtained from ^{13}C-labelling experiment. a, ^{1}H-NMR spectrum of catholyte after $^{13}CO_2RR$ on 34% N-C/Cu cathodes by applying 300 mA cm^{-2} in 1 M KOH. **b**,**c**, The corresponding enlarged ^{1}H-NMR spectra demonstrating that ethanol is produced from $^{13}CO_2RR$.

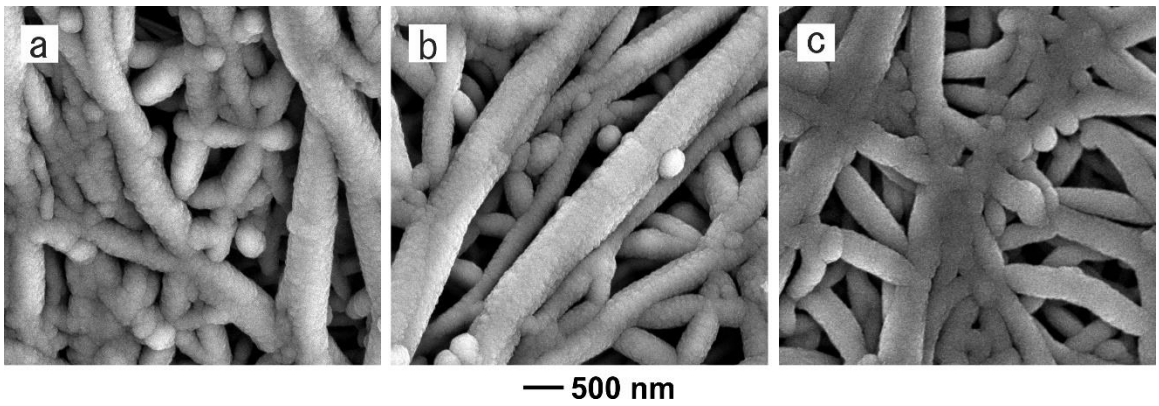

Supplementary Figure 33 | SEM images of catalysts: 26% N-C/Cu (a), 39% N-C/Cu (b), and C/Cu (c).

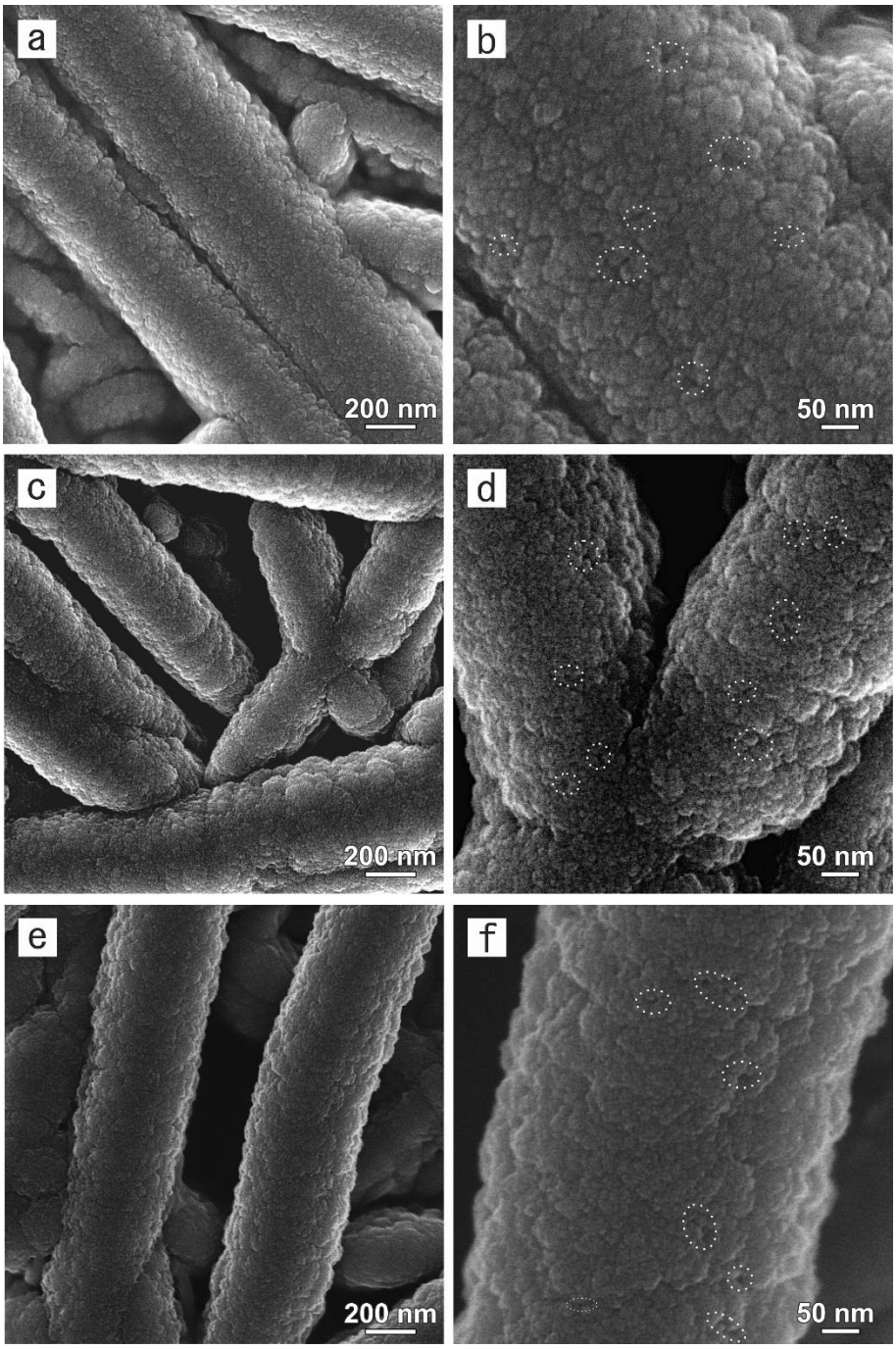

Supplementary Figure 34 | SEM images of catalysts: 26% N-C/Cu (a,b), 39% N-C/Cu (c,d), and C/Cu (e,f). The holes on N-C and C layers are marked using dotted lines.

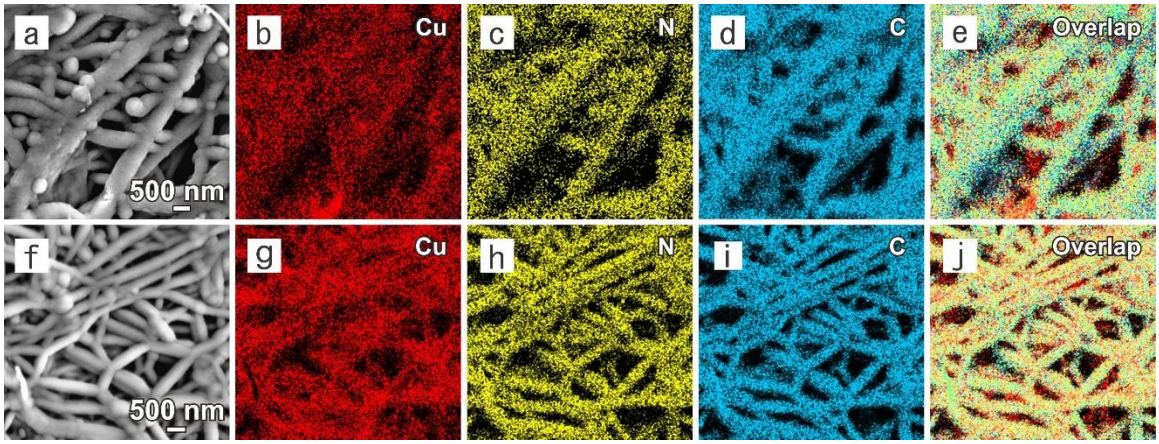

Supplementary Figure 35 | Structural and compositional analyses of the N-C/Cu catalysts on PTFE. a-e, SEM image (**a**) and the corresponding EDX elemental mapping (**b-e**) of Cu, N, and C for 26% N-C/Cu. **f-j**, SEM image (**f**) and the corresponding EDX elemental mapping (**g-j**) of Cu, N, and C for 39% N-C/Cu.

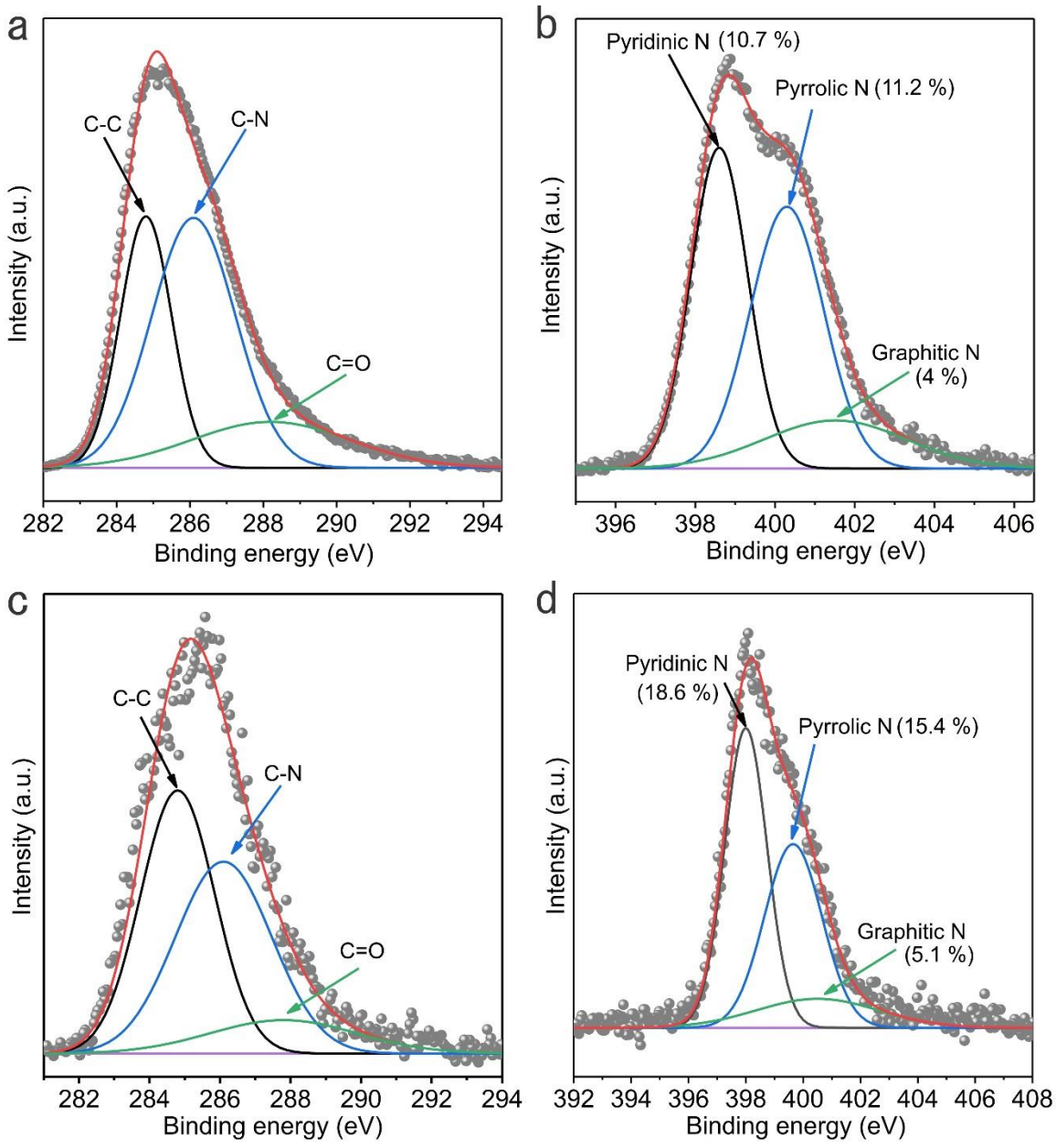

Supplementary Figure 36 | XPS analysis for different N-C/Cu catalysts on PTFE. a,**b**, High-resolution C 1s (**a**) and N 1s (**b**) spectra for 26% N-C/Cu catalyst on PTFE. **c**,**d**, High-resolution C 1s (**c**) and N 1s (**d**) spectra for 39% N-C/Cu catalyst on PTFE.

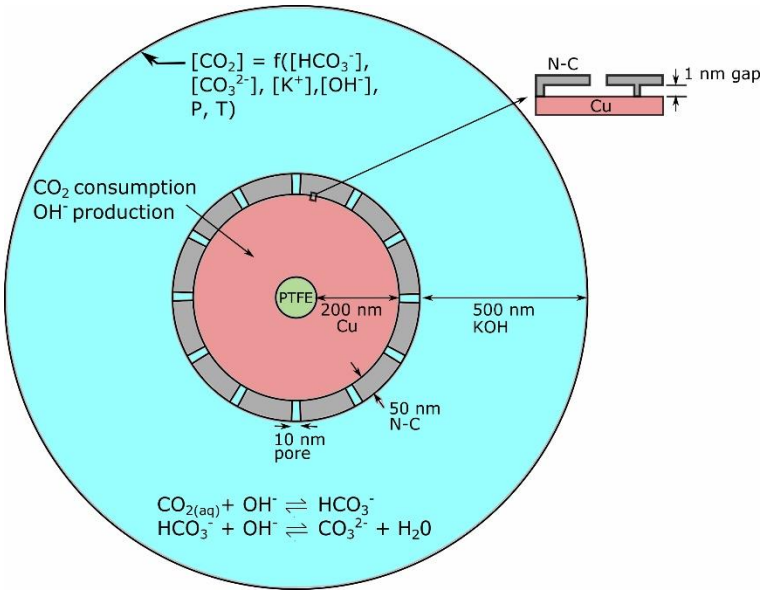

Supplementary Figure 37 | Schematic of CO_2RR configuration for N-C on Cu catalyst layer.

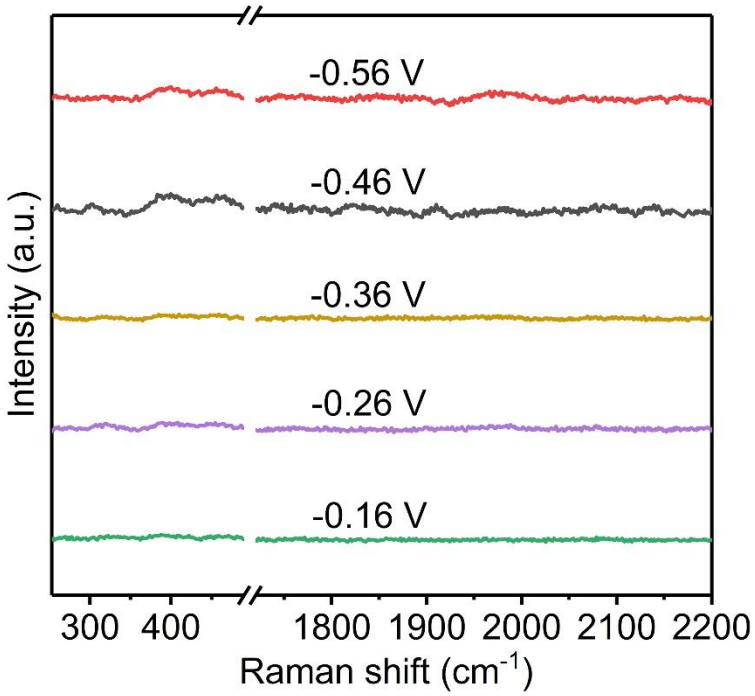

Supplementary Figure 38 | In situ Raman spectra of 34% N-C/Cu in Ar-saturated KOH under different applied potentials.

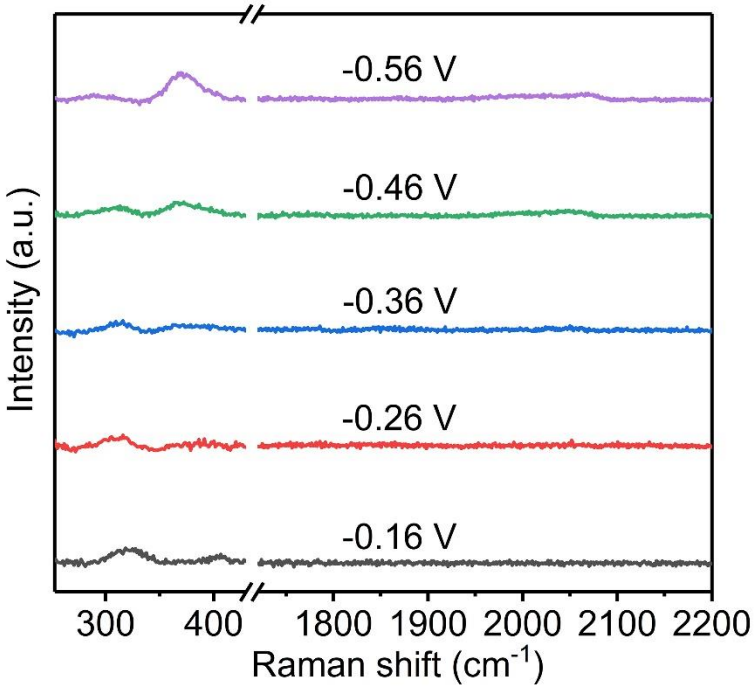

Supplementary Figure 39 | In situ Raman spectra of Cu catalyst during CO_2RR under different applied potentials.

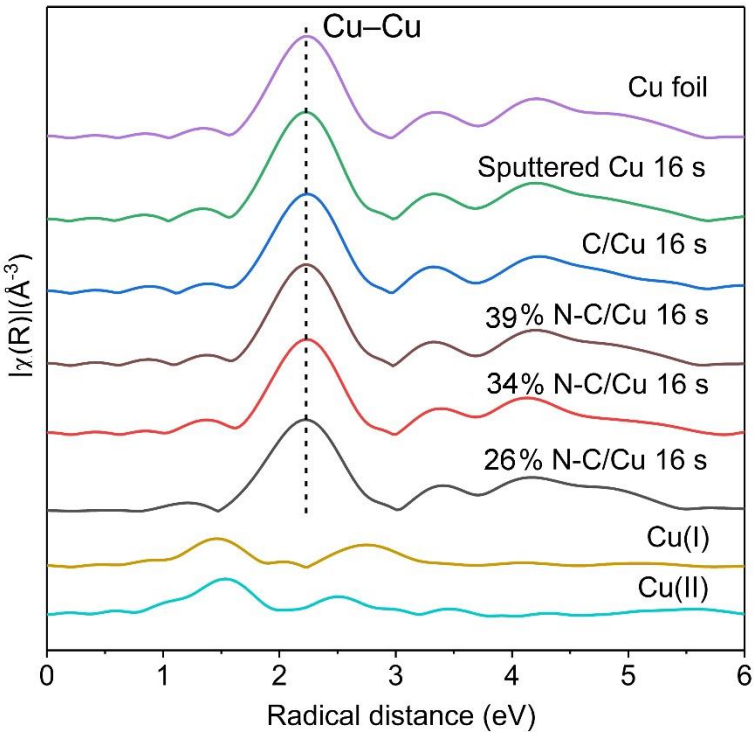

Supplementary Figure 40 | Operando Cu K-edge extended X-ray adsorption fine structure (EXAFS) spectra of different catalysts during CO_2RR by applying 300 mA cm^{-2}. Bulk Cu foil, CuO, and Cu_2O are listed as references.

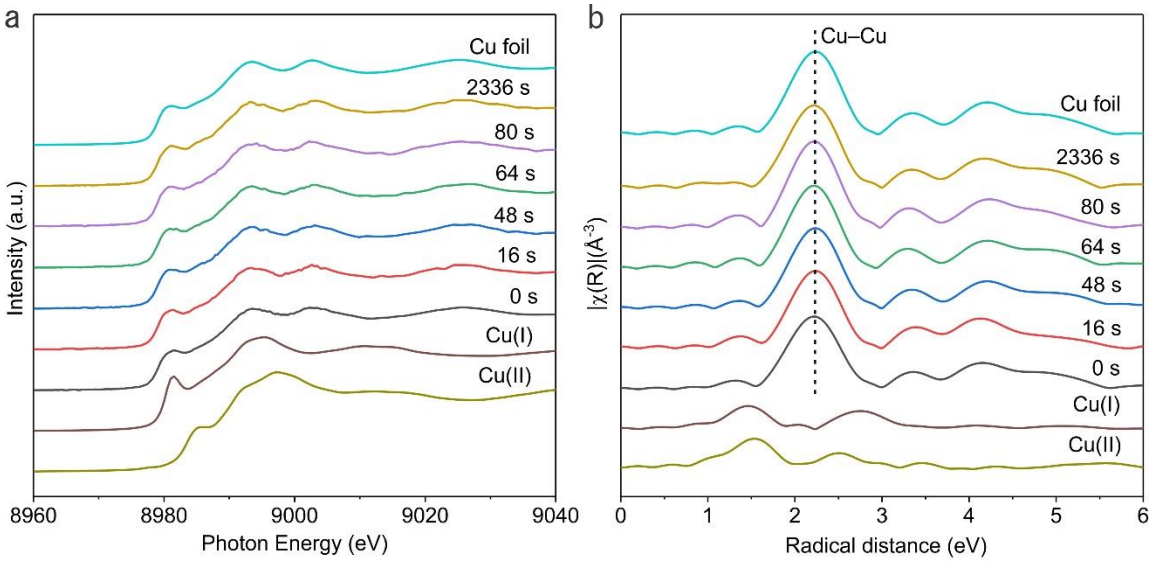

Supplementary Figure 41 | Operando XAS characterizations. a,**b**, Operando Cu K-edge XANES (**a**) and EXAFS spectra (**b**) of 34% N-C/Cu catalyst during CO_2RR by applying 300 mA cm^{-2}. Bulk Cu foil, CuO, and Cu_2O are listed as references.

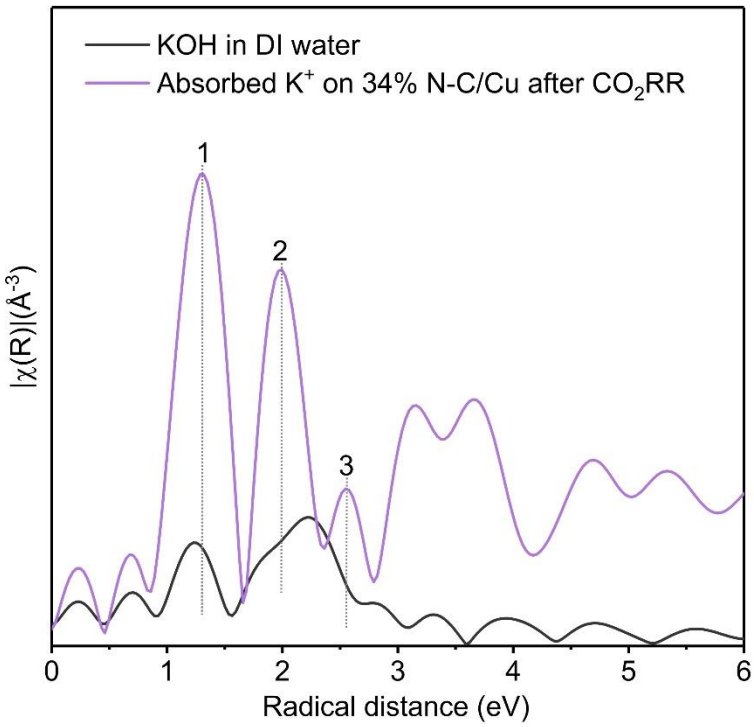

Supplementary Figure 42 | Potassium K-edge EXAFS spectra of KOH dissolved in DI water and absorbed K+ on 34% N-C/Cu after CO_2RR with KOH as the electrolyte. After CO_2RR, the catalyst was rinsed using DI water to remove the KOH solution on the surface of catalyst and was dried by N_2 before ex-situ XAS measurement. The peaks 1, 2, and 3 can be assigned as adsorbed K^+ on C, K^+-OH^-, and adsorbed K^+ on Cu, respectively[1-4].

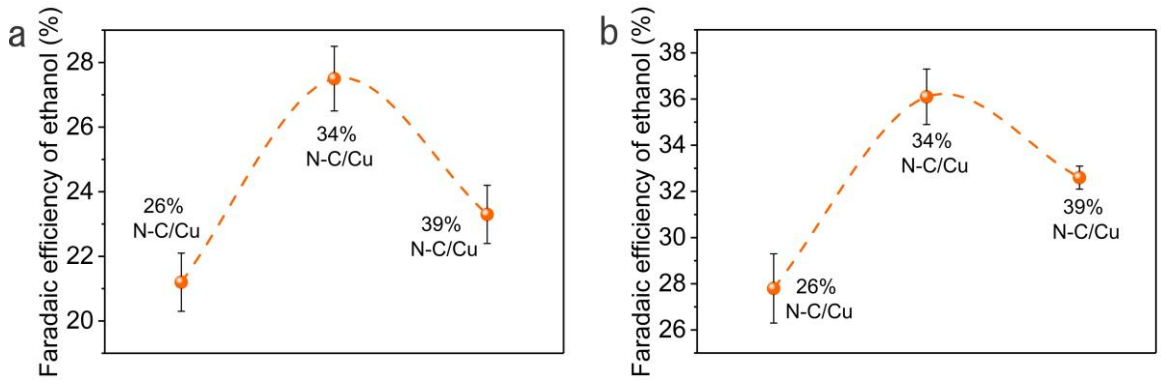

Supplementary Figure 43 | Comparison of ethanol FEs on different types of N-C/Cu catalysts under different current densities: a, 100 mA cm^{-2}; b, 200 mA cm^{-2}. Error bars represent the standard deviation of measurements based on three independent samples.

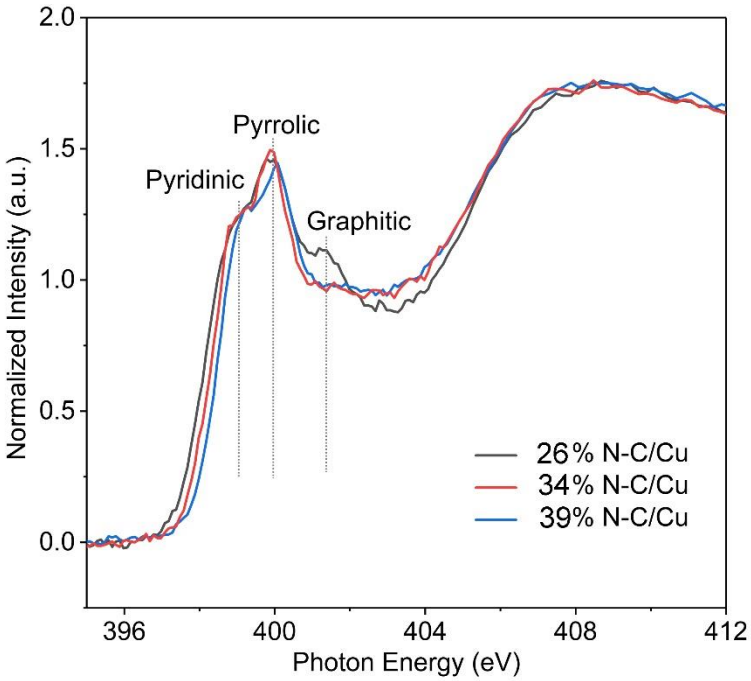

Supplementary Figure 44 | Nitrogen K-edge XANES spectra of different N-C/Cu catalysts recorded in PFY mode.

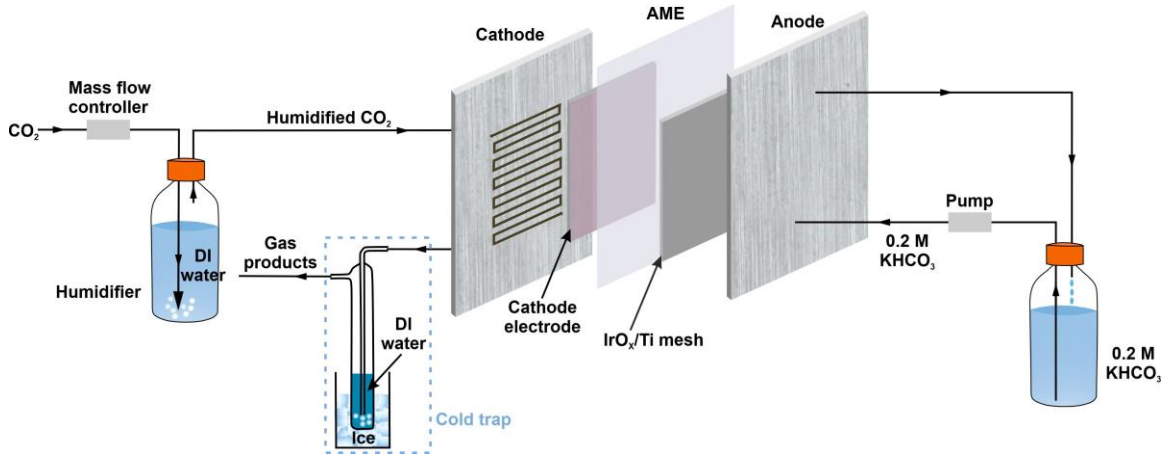

Supplementary Figure 45 | Schematic diagram of the MEA system. The total geometric area of the flow field in the cathode is 5 cm^2, where 45% is the gas channel area and 55% is the land area.

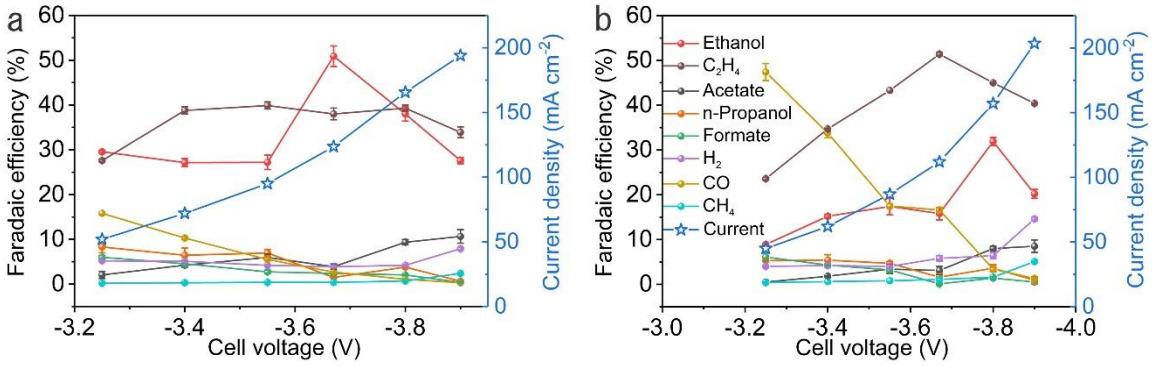

Supplementary Figure 46 | CO_2RR performance in MEA system. a,**b**, FEs of different products and current densities in CO_2RR on 34% N-C/Cu catalyst (**a**) and Cu catalyst (**b**) under different cell voltages. The color scheme in (**b**) also applies to panel (**a**). Error bars represent the standard deviation of measurements based on three independent samples.

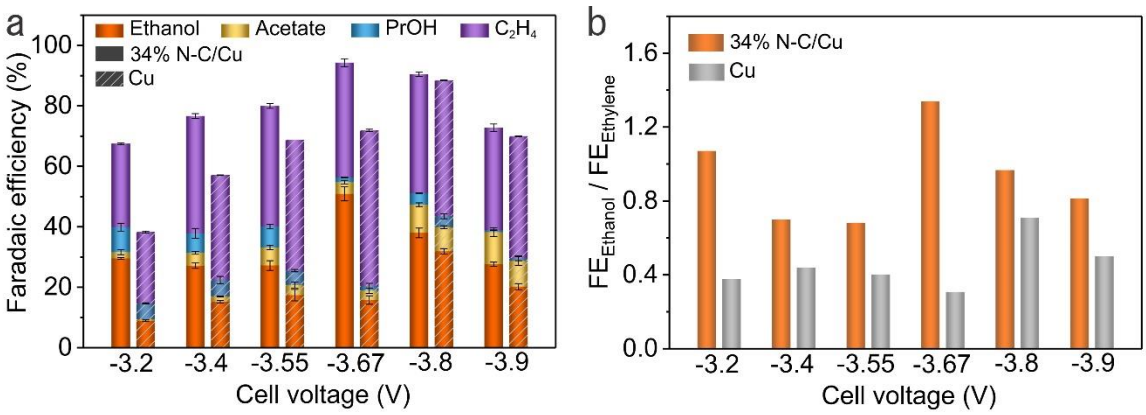

Supplementary Figure 47 | CO_2RR performance comparisons in MEA system. a, FEs of C_{2+} products on 34% N-C/Cu and Cu (the hatched bars) catalysts under different cell voltages. Error bars represent the standard deviation of measurements based on three independent samples. **b**, Comparison of the ratios of $FE_{ethanol}$ to $FE_{ethylene}$ on 34% N-C/Cu and Cu catalysts under different cell voltages.

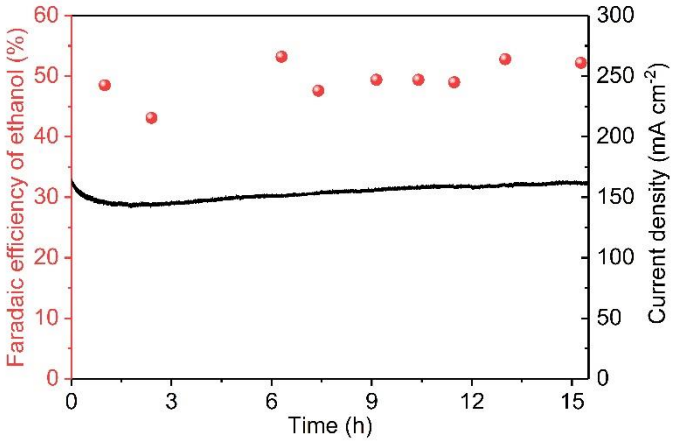

Supplementary Figure 48 | Performance test of CO_2RR to ethanol in MEA system during 15 hours of electrolysis under the full-cell voltage of -3.67 V.

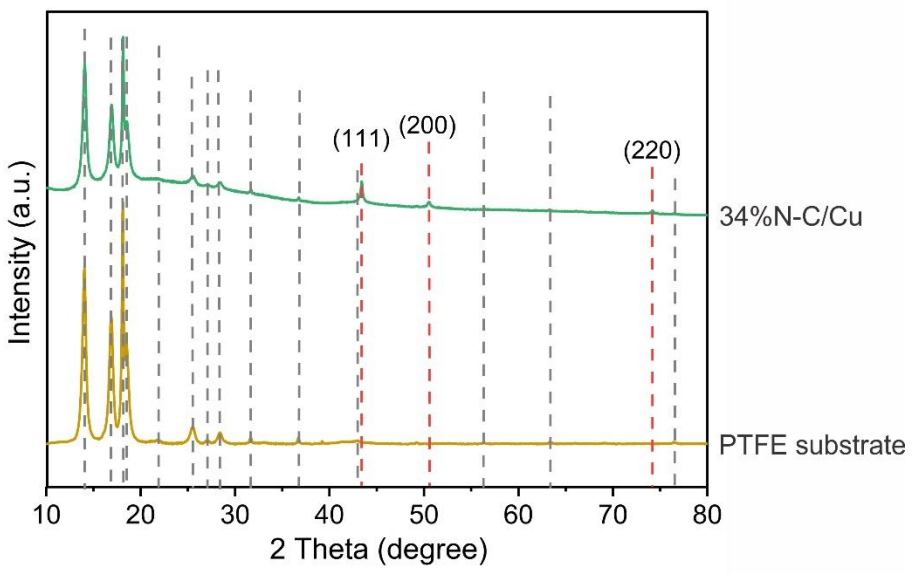

Supplementary Figure 49 | XRD patterns for 34% N-C/Cu catalyst on PTFE after 15 h electrolysis and bare PTFE substrate. The peaks marked by gray and red dot lines come from PTFE substrate and Cu, respectively.

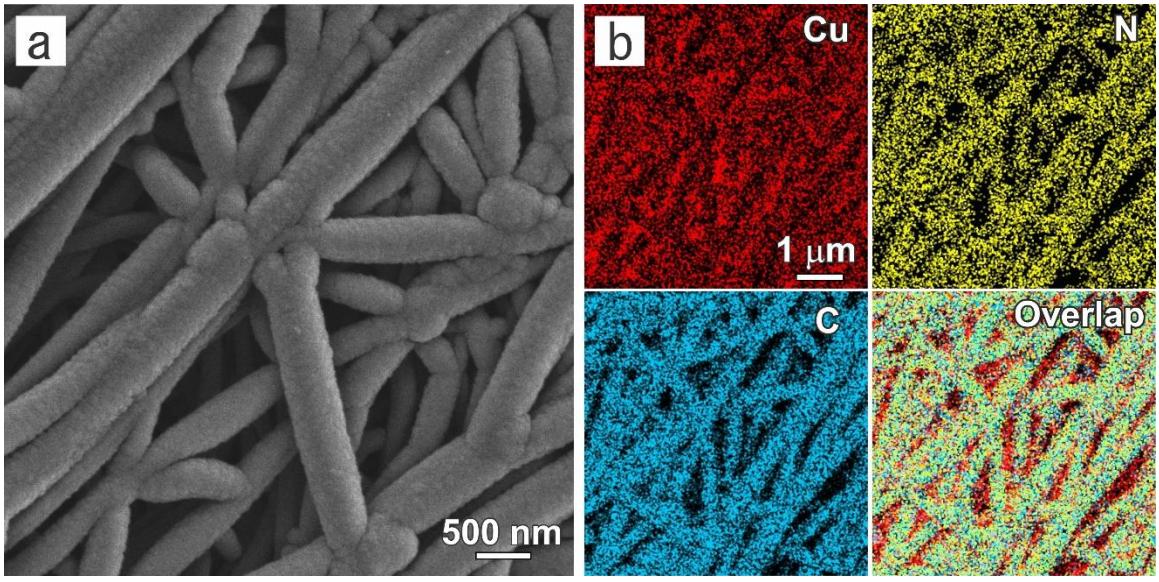

Supplementary Figure 50 | Structural and compositional analyses of the 34% N-C/Cu catalyst on PTFE after 15 h electrolysis. a,**b**, Low magnification SEM image (**a**) and EDX elemental mapping of Cu, N, and C (**b**) for 34% N-C/Cu catalyst on PTFE after 15 h electrolysis.

Supplementary Table 1 | Comparison of ethanol FE for reports with the total current density higher than 10 mA cm^{-2}.

Catalysts	$FE_{ethanol}$ (%)	$J_{geometric, ethanol}$ (mA cm^{-2})	Cathodic $EE_{ethanol}$ (%)	References
N-C/Cu	52 ± 1	156 ± 3	31	This work
Boron-doped Cu	27 ± 1	19 ± 1	13	*Nat. Chem.* **19**, 974-980 (2018)
Cu_2S-Cu	25	100	13	*Nat. Catal.* **1**, 421-428 (2018)
CuAg	25	75	15	*J. Am. Chem. Soc.* **140**, 5791-5797 (2018)
CuDAT-wire	27	75	16	*ACS Catal.* **7**, 3313-3321 (2017)
N-GQD	16	23	9	*Nat. Commun*. **7**, 13869 (2016)
Molecule-Cu	41	124	23	*Nat. Catal.* **3**, 75-82 (2020)

Supplementary Table 2 | Activation energies (E_a) and enthalpy changes (ΔH) of CO dimerization on Cu, C/Cu, and N-C/Cu.

	E_a (eV)	ΔH (eV)
Cu	0.72	0.65
C/Cu	0.77	0.62
N-C/Cu	0.70	0.52

Supplementary Table 3 | Reaction energies of the intermediate state (HOCCH*) to CCH* (ethylene pathway) and HOCHCH* (ethanol pathway) on Cu, C/Cu, and N-C/Cu, respectively.

	Ethylene pathway (eV)	Ethanol pathway (eV)
Cu	-0.09	-0.11
C/Cu	-0.09	-0.20
N-C/Cu	0.07	-0.03

Supplementary Table 4 | Reaction energies of the ethylene and ethanol pathways and energy differences of the ethanol and ethylene pathways on Cu(100) and N-C/Cu(100), respectively. All the energies are in eV.

	Ethylene pathway (eV)	Ethanol pathway (eV)	Ethanol pathway-Ethylene pathway (eV)
Cu(100)	-0.26	-0.48	-0.22
N-C/Cu(100)	-0.47	-0.76	-0.29

We have also considered the confinement effect of N-C layer on Cu(100) by calculating the reaction energies of the ethylene and ethanol pathways on Cu(100) and N-C/Cu(100), as shown in Supplementary Table 4. The results show that, compared to Cu(100), N-C/Cu(100) also tends to improve the ethanol selectivity *vs.* ethylene.

Supplementary Table 5 | Reaction energies of ethylene and ethanol pathways and activation energies (E_a) and enthalpy changes (ΔH) of CO dimerization on Cu with different layers of graphite. All the energies are in eV.

Layer	Ethylene pathway	Ethanol pathway	CO dimerization	
			E_a	ΔH
1	-0.09	-0.20	0.77	0.62
2	-0.10	-0.21	0.77	0.63
3	-0.10	-0.21	0.77	0.63

To understand the effects of different layers of graphite in CO_2RR, we investigated CO dimerization, HOCCH* to CCH* (ethylene pathway), and HOCCH* to HOCHCH* (ethanol pathway) on C/Cu with different layers of graphite carbon (Supplementary Table 5 and Supplementary Fig. 7). Compared to the case of graphene on Cu, the results suggest that adding multi-layer graphite on Cu almost does not change the energies of CO dimerization, nor does it change the reaction energies of the ethylene and ethanol pathways – these energies are related to the confinement effect and the electron-donating capability of the catalyst. Therefore, using a monolayer model is sufficient to describe the confinement effect, together with the electronic properties and the electron-donating capability. To simplify model, we use graphene and N-doped graphene for calculations in the manuscript.

Supplementary Table 6 | Energy differences of the ethanol and ethylene pathways ($E_{\text{ethanol pathway}}$-$E_{\text{ethylene pathway}}$), activation energies ($E_a$ (OC-CO)), and enthalpy changes (ΔH (OC-CO)) of CO dimerization using the charged water model and 1.0 M KOH using GCQM. All the energies are in eV.

Methods	Energy (eV)	Cu	C/Cu	N-C/Cu
Charged water model	$E_{\text{ethanol pathway}}$-$E_{\text{ethylene pathway}}$	-0.02	-0.12	-0.11
	E_a (OC-CO)	0.72	0.77	0.70
	ΔH (OC-CO)	0.65	0.62	0.52
1.0 M KOH using GCQM	$E_{\text{ethanol pathway}}$-$E_{\text{ethylene pathway}}$	0.09	-0.08	-0.01
	E_a (OC-CO)	0.82	0.85	0.77
	ΔH (OC-CO)	0.78	0.73	0.61

To consider the effect of the double layer under negative potentials, we implemented the grand canonical quantum mechanics (GCQM) method[5] in JDFTX (ref. 6). We adapted the settings in the paper of Goddard and co-workers[7]. We set the ions to be 1.0 M KOH and the applied potential to be 0 V *vs.* standard hydrogen electrode (SHE). A comparison between the charged water model and the GCQM method is provided in Supplementary Table 6. There are slight differences in absolute values, but the trends are in agreement: N-C/Cu is the best for CO dimerization, and both C/Cu and N-C/Cu favor ethanol. The high barrier of CO dimerization on C/Cu limits selectivity towards C_2 products, agreeing with our experiment results.

Supplementary Table 7 | Stabilities with respect to the ground state (Stability) and reaction energies of ethylene and ethanol pathways on N-C/Cu with different distances between N-C layer and Cu layer ($d_{N\text{-}C/Cu}$).

$d_{N\text{-}C/Cu}$ (Å)	Stability	Energy (eV)		
		Ethylene pathway	Ethanol pathway	$E_{ethanol\ pathway}$-$E_{ethylene\ pathway}$
6.42	0.45	0.02	-0.24	-0.26
7.42	0.00	0.07	-0.03	-0.1
8.42	0.19	0.02	-0.01	-0.03
9.42	0.37	0.02	-0.11	-0.13

In our main calculations, the distance between N-C layer and Cu layer ($d_{N\text{-}C/Cu}$) in the model are 7.42 Å. We obtained this distance by relaxing the system starting from a variety of different initial structures. We set $d_{N\text{-}C/Cu}$ to take on values ranging from 6.42 Å to 9.42 Å, fixed the graphene layer, and allowed the other atoms to be relaxed. The stabilities of these systems are shown in Supplementary Table 7. The results suggest that either decreasing or increasing the $d_{N\text{-}C/Cu}$ from 7.42 Å leads to a decrease in stability, leading to the conclusion that 7.42 Å is the equilibrium distance between N-C layer and Cu layer due to the highest stability of the system.

We calculated the reaction energies of ethylene pathway (HOCCH* to CCH*) and ethanol pathways (HOCCH* to HOCHCH*) on N-C/Cu with the distances between N-C layer and Cu layer changing from 6.42 Å to 9.42 Å (Supplementary Table 7). Similar to the results with the optimal $d_{N\text{-}C/Cu}$ (7.42 Å) for our main calculations, N-C/Cu still tends to improve the ethanol selectivity *vs.* ethylene with the $d_{N\text{-}C/Cu}$ range of 6.42 Å to 9.42 Å with respect to Cu (Supplementary Table 2). Therefore, the calculation results demonstrate that, ethanol selectivity can be promoted in N-C/Cu with the $d_{N\text{-}C/Cu}$ range of 6.42 Å to 9.42 Å, compared to bare Cu.

In addition, with the change in dN-C/Cu, the geometries of the key intermediate HOCCH*, the intermediate CCH*, and the intermediate HOCHCH* don't change significantly (Supplementary Figs. 10-12).

Supplementary Table 8 | Indexes, filenames of the xyz files in paper of Deringer et al. (ref. 8), indexes of the randomly doped nitrogen, number of carbon atoms, number of nitrogen atoms, and formation energies per atom (E_f) of the top 10 most stable structures.

Index	Filename	Index of the randomly doped nitrogen	Number of carbon atoms	Number of carbon atoms	E_f (eV)
1	DFT_relaxed_02_1.xyz	28,6,33,1,0,23,11,18,33,18	27	6	0.07
2	DFT_relaxed_06_2.xyz	25,13,5,20,42,26,25,15,17,12,19,33	32	9	0.11
3	DFT_relaxed_02_1.xyz	26,22,12,34,11,1,24,17,29,3	25	8	0.12
4	DFT_relaxed_01_1.xyz	11,12,4,25,42,36,30,36,6,22,6,40	33	8	0.13
5	DFT_relaxed_01_1.xyz	35,36,18,27,17,8,42,9,11,35,39,15	32	9	0.14
6	DFT_relaxed_06_2.xyz	5,16,24,3,42,2,28,13,36,10,12,12	32	9	0.14
7	DFT_relaxed_06_2.xyz	24,9,5,7,22,33,21,24,8,15,37,36	32	9	0.18
8	DFT_relaxed_06_2.xyz	31,10,15,39,20,23,10,40,27,11,7,4	32	9	0.18
9	DFT_relaxed_02_1.xyz	14,1,3,27,26,34,23,28,7,19	25	8	0.18
10	DFT_relaxed_09_3.xyz	8,24,16,11,3,9,40,28,12,15,29,28	30	9	0.20

Supplementary Table 9 | Reaction energies of ethanol and ethylene pathways on the top 10 most stable amorphous N-doped carbon structures. Reconstructed structures are labeled TRUE, while unreconstructed ones are labeled FALSE. Only the reaction energies of unreconstructed structures are used in the calculation of average reaction energies. All the energies are in eV.

	Ethanol pathway	Ethylene pathway	
1	-0.37	0.22	FALSE
2	0.05	0.01	FALSE
3	-0.35	0.22	FALSE
4	0.11	0.18	FALSE
5	-0.68	-0.15	FALSE
6	-1.01	-0.49	TRUE
7	-0.09	-0.78	FALSE
8	0.14	0.17	FALSE
9	0.28	0.18	FALSE
10	-2.02	0.09	TRUE
average	-0.12	0.01	

Supplementary Table 10 | Product FEs for different nanocatalysts under different applied current densities in CO_2RR. Error bars represent the standard deviation of measurements based on three independent samples.

Catalysts	J_{total} (mA cm^{-2})	$FE_{acetate}$ (%)	$FE_{ethanol}$ (%)	$FE_{ethylene}$ (%)	$FE_{n\text{-}propanol}$ (%)	$FE_{formate}$ (%)	FE_{CO} (%)	$FE_{methane}$ (%)	$FE_{hydrogen}$ (%)
Cu	100	1.4±0.4	17.7±0.4	45.8±2.5	5.6±0.5	7.5±1.1	6.2±0.4	0.7±0.1	11.9±0.5
	200	1.8±0.3	24.9±1.3	51.7±0.7	4.5±0.6	4.5±0.9	2.8±0.3	1±0.1	9.2±0.5
	300	2.3±0.3	31.4±2.7	48.2±1.7	2.6±0.2	1.8±0.5	1.4±0.3	1.7±0.2	8.9±0.3
34% N-C/Cu	100	3.2±0.3	27.5±1	45.1±3.4	7.7±0.2	5.4±0.8	2.9±0.6	0.4±0.1	6.6±0.8
	200	2.6±0.2	36.1±1.2	45.1±1.7	3.7±0.8	2.7±0.1	1.2±0.3	1.1±0.1	5.6±0.1
	300	2.3±0.8	52.3±0.7	37.5±0.5	1.4±0.1	1.7±0.4	0.3±0.1	1.2±0.2	7.4±0.9
26% N-C/Cu	100	2.7±0.4	21.2±0.9	46.2±2	5.9±1	7.5±0.8	4.3±0.4	0.6±0.2	8.1±0.3
	200	2.4±0.7	27.8±1.5	52.2±0.4	4.2±0.8	2.3±0.9	1.2±0.4	1±0.1	6±0.2
	300	2±0.5	42.6±1.5	43.3±1.5	0.9±0.2	1.4±0.2	0.6±0.2	2.1±0.8	7.8±1.3
39% N-C/Cu	100	1.9±0.4	23.3±0.9	48.8±0.4	8.6±1.9	5.1±0.4	3.8±0.7	0.7±0.1	10±0.3
	200	3.1±0.3	32.6±0.5	46.7±1.3	3.7±0.3	2.9±0.2	1.7±0.3	0.7±0.1	6.4±0.1
	300	3.6±0.2	43.7±0.8	44.2±1.5	2.9±0.4	2.4±0.4	0.8±0.1	2.5±0.1	6.4±0.1
C/Cu	100	1.8±0.3	17.2±1.1	41.8±1.8	6.5±1.5	16.3±1.4	3.7±0.6	0.5	7.4±0.3
	200	2.7±0.1	25±1	49.3±0.8	2.2±1.4	3.5±0.3	1.5±0.4	2.2±0.2	8.6±0.2
	300	2.5±0.3	30.5±2.2	33.8±1.6	1.8±0.4	2.9±0.3	0.6±0.1	8.4±0.3	20.5±0.8

Supplementary Table 11 | CO_2 adsorption energies ($CO_2(g) \rightarrow *CO_2$), reaction energies of CO_2 activation ($*CO_2 \rightarrow *COOH$), reaction energies of *COOH hydrogenation ($*COOH \rightarrow *CO$), and reaction energies of ($H^+ + e^- \rightarrow * H$) in HER on N-C/Cu and Cu. All the energies are in eV.

	N-C/Cu	Cu
$CO_2(g) \rightarrow *CO_2$	0.60	1.17
$*CO_2 \rightarrow *COOH$	0.56	0.44
$*COOH \rightarrow *CO$	-0.50	-0.54
$H^+ + e^- \rightarrow * H$	-0.05	-0.06

The rate-determining step of CO_2RR is widely accepted as the first a few steps of CO_2RR, including CO_2 adsorption, CO_2 activation, and *COOH hydrogenation[9]. Chan, Nørskov, and co-workers[10] reported that after C-C coupling, the ensuing elementary steps are downhill. Therefore, the competing steps are HER and the first a few steps of CO_2RR. To understand the effect of confinement on HER in N-C/Cu, we investigated CO_2 adsorption, CO_2 activation, *COOH hydrogenation, and reaction energies of ($H^+ + e^- \rightarrow * H$) in HER on Cu and N-C/Cu (Supplementary Table 11). Our results suggest that, compared to the case of Cu, CO_2 adsorption ($CO_2(g) \rightarrow *CO_2$) is enhanced due to the confinement effect of N-C/C. In contrast, the energies of other steps ($*CO_2 \rightarrow *COOH$ and $*COOH \rightarrow *CO$) and reaction energies of ($H^+ + e^- \rightarrow * H$) in HER on N-C/Cu are close to these on Cu. Therefore, introducing the N-C layer does not promote HER; its impact is instead to promote CO_2RR activity. These results are consistent with our experiment observation – H_2 FEs decrease after introducing N-C layer on Cu (Supplementary Table 10).

Supplementary Table 12 | Cu_{ECSA} determined by Pd_{UPD} method for different samples.

	Cu_{ECSA} (cm^2)
Cu	6.42
26% N-C/Cu	4.41
34% N-C/Cu	5.91
39% N-C/Cu	5.65

Supplementary Table 13 | Local pH at Cu surfaces for cases with and without the N-C layer.

	With N-C on Cu	Only Cu
Local pH	13.9	13.9

Supplementary Table 14 | Adsorption energies of CO (E_{CO}) on pure Cu, C/Cu, and N-C/Cu. The adsorption energies are calculated with structures in Supplementary Fig. 2 with two CO molecules, and the energies listed below are the average adsorption energies.

	E_{CO} (eV)
Cu	-0.48
C/Cu	0.10
N-C/Cu	-0.60

Supplementary References

1. van Oversteeg, C. H. M., Doan, H. Q., de Groot, F. M. F. & Cuk, T. In situ x-ray absorption spectroscopy of transition metal based water oxidation catalysts. *Chem. Soc. Rev.* **46**, 102-125 (2017).
2. Li, Q et al. A unified intermediate and mechanism for soot combustion on potassium-supported oxides. *Sci. Rep.* **4**, 4725 (2014).
3. Kiguchi, M., Entani, S., Saiki, K., Inoue, H. & Koma, A. Two types of epitaxial orientations for the growth of alkali halide on fcc metal substrates. *Phys. Rev. B* **66**, 155424 (2002).
4. Kiguchi, M., Yoshikawa, G., Ikeda, S. & Saiki, K. Electronic properties of metal-induced gap states formed at alkali-halide/metal interfaces. *Phys. Rev. B* **71**, 153401 (2005).
5. Sundararaman, R., Goddard III, W. A. & Arias, T. A. Grand canonical electronic density-functional theory: Algorithms and applications to electrochemistry. *J. Chem. Phys.* **146**, 114104 (2017).
6. Sundararaman, R. et al. JDFTx: Software for joint density-functional theory. *SoftwareX* **6**, 278-284 (2017).
7. Xiao, H., Cheng, T. & Goddard III, W. A. Atomistic mechanisms underlying selectivities in C_1 and C_2 products from electrochemical reduction of CO on Cu(111). *J. Am. Chem. Soc.* **139**, 130-136 (2017).
8. Deringer, V. L. et al. Computational surface chemistry of tetrahedral amorphous carbon by combining machine learning and density functional theory. *Chem. Mater.* **30**, 7438-7445 (2018).
9. Chernyshova, I. V., Somasundaran, P. & Ponnurangam, S. On the origin of the elusive first intermediate of CO_2 electroreduction. *Proc. Natl. Acad. Sci.* **115**, E9261-E9270 (2018).
10. Liu, X. et al. pH effects on the electrochemical reduction of $CO_{(2)}$ towards C_2 products on stepped copper. *Nat. Commun.* **10**, 32 (2019).